Olivia Kettner, BSc

Influence of the Polyfluorene Side Chain Geometry on the Physics of Fullerene Blend Solar Cells

MASTER THESIS

For obtaining the academic degree
Diplom-Ingenieurin

Master Programme of
Technical Physics

Graz University of Technology

Graz University of Technology

Supervisor:

Dipl.-Phys. Dr.rer.nat. Bettina Friedel

Co-Supervisor:

Univ.-Prof. Ph.D. Peter Hadley

Institute of Solid State Physics

Graz, November 2014

EIDESSTATTLICHE ERKLÄRUNG

AFFIDAVIT

Ich erkläre an Eides statt, dass ich die vorliegende Arbeit selbstständig verfasst, andere als die angegebenen Quellen/Hilfsmittel nicht benutzt, und die den benutzten Quellen wörtlich und inhaltlich entnommenen Stellen als solche kenntlich gemacht habe. Das in TUGRAZonline hochgeladene Textdokument ist mit der vorliegenden Diplomarbeit identisch.

I declare that I have authored this thesis independently, that I have not used other than the declared sources/resources, and that I have explicitly indicated all material which has been quoted either literally or by content from the sources used. The text document uploaded to TUGRAZonline is identical to the present diploma thesis.

Datum / Date	Unterschrift / Signature

Acknowledgements

At this point I would like to express my gratitude to all people who contributed to this work. First and foremost to my supervisor Dipl.-Phys. Dr.rer.nat. Bettina Friedel, for introducing me to this topic, the friendly guidance and the constructive criticism. Special thanks also to my co-supervisor Univ.-Prof. Ph.D. Peter Hadley for his helpful advice. Also thanks to Roland Resel and his group for performing measurements on my samples at BESSY and the people from the Carvendish Laboratory in Cambridge for the support and assistance during performing measurements there. A special thanks to Elisabeth Stern for fighting with all the administrative barriers. I would also like to thank my colleagues at the Institute of Solid State Physics for a lot of fruitful discussions and during coffee breaks.

Furthermore, I would like to thank the FWF for the funding of my project, which also gave me the opportunity to participate at the EMRS spring meeting.

Finally I would like to thank my family, especially my parents, and friends for permanent encouragement and mental support during my studies.

Abstract

Co-polymers based on fluorene and thiophene monomer units are attractive for photovoltaic device fabrication, because of high charge carrier mobility and broad absorption in the visible range. In this work, three types of poly(9,9‘-dioctyl-fluorene-co-bithiophene) (F8T2) with different ordered side chains were investigated. The side chains of F8T2 were modified between straight alkyl groups (octyl groups) and branched alkyl groups (2-ethylhexyl groups). By keeping same number of carbon atoms in the side-chain but exchanging its geometry, different interchain distance of the backbone was achieved, which influences the crystallization tendency. F8T2 with octyl side chains has a high tendency to crystallize. Incorporation of 2-ethylhexyl groups leads to a more amorphous polymer morphology because of the increased interplanar distance of neighbouring polymer chains. For the third polymer, fluorenes with both, 2-ethylhexyl and octyl side chains were statistically incorporated onto the main chain. This breaks the symmetry of the side chains and therewith disturbs their regularity. Bulk-heterojunction blends with the F8T2’s as donor and the fullerene derivative indene-C60 bisadduct (ICBA) as acceptor were fabricated and used for all investigations. To examine the impact of the different ordered side chains on the photophysics, the emission behaviour was investigated by photoluminescence (PL) spectroscopy. Their comparison showed efficient quenching of the emission for donor/acceptor blends, compared to donor-only films. This desired behaviour represents one potential evidence of efficient exciton dissociation and charge separation. Also optical absorption spectra in the ultraviolet and visible wavelength range were recorded and showed an absorption maximum around 450 nm, which is typical for F8T2. Further, time-correlated single photon counting (TCSPC) was used to compare the fluorescence decay of the excited states. The emission dynamics revealed different behaviour for F8T2s depending on the substituted side-chains. With electroluminescence studies, variations in position and intensity of charge transfer (CT) states were observed, which have considerable impact on the performance of organic solar cells, because of their critical role in the separation of photo-generated charge carriers. Investigations further revealed significant changes in photovoltaic device physics. The polymer with straight and branched side-chains is the most promising candidate for solar cells, as it delivers the highest photocurrents. Atomic force microscopy revealed different degrees of donor-acceptor phase separation for the three used polymers.

Kurzfassung

Copolymere, die aus Fluoren und Thiophen Monomer Einheiten bestehen, eignen sich für die Herstellung photovoltaischer Bauteile auf Grund ihrer guten Ladungsträgermobilität und ihrer Absorptionsfähigkeit im sichtbaren Wellenlängenbereich. In dieser Arbeit wurden drei verschiedene Typen von poly(9,9‘-dioctyl-fluorene-co-bithiophene) (F8T2) mit unterschiedlich angeordneten Seitenketten untersucht. Als Seitenketten wurden gerade alkyl Gruppen (oktyl Gruppen) und verzweigte alkyl Gruppen (2-ethylhexyl Gruppen) verwendet. Durch diese Modifikation der Seitenketten, bei der die Anzahl an Kohlenstoffatomen beibehalten aber die Geometrie verändert wurde, werden unterschiedliche Abstände zwischen den Polymer Backbones erreicht, was die Tendenz zur Kristallisation beeinflusst. F8T2 hat eine hohe Tendenz zur Kristallisation, während das Verwenden von 2-ethylhexyl Gruppen zu einer amorpheren Morphologie des Polymers führt, da der interplanare Abstand zwischen benachbarten Polymerketten zu nimmt. Für das dritte Polymer wurden Fluorene mit 2-ethylhexyl und oktyl Seitenketten, statistisch verteilt, mit der Hauptkette verbunden. Dadurch wird die Symmetrie der Seitenketten gebrochen und ihre Ordnung gestört. Bulkheterojunction Filme mit F8T2 als Donor Material und dem Fulleren Derivat indene-C60 bisadduct (ICBA) als Akzeptor wurden hergestellt und für Untersuchungen herangezogen. Um den Einfluss der unterschiedlich geordneten Seitenketten auf die Photophysik zu untersuchen wurde das Emissionsverhalten durch Photolumineszenz Messungen untersucht. Der Vergleich der aufgenommenen Spektren von Donor/Akzeptor Filmen mit Donor Filmen zeigt effiziente Fluoreszenzauslöschung. Dieses Verhalten ist ein potenzieller Indikator für die effiziente Dissoziation von Exzitonen und Separation von Ladungsträgern. Absorptionsspektren wurden im ultravioletten und sichtbaren Wellenlängenbereich aufgenommen und zeigen ein Absorptionsmaximum bei etwa 450 nm, was typisch für F8T2 ist. Weiters wurden zeitkorrelierte Einzelphotonenmessungen durchgeführt, um die Fluoreszenzabnahme der angeregten Zustände zu vergleichen. Die Emissionsdynamik zeigte unterschiedliches Verhalten für die Polymere in Abhängigkeit von den verwendeten Seitenketten. Durch

Elektrolumineszenz Messungen wurden Unterschiede in der Position und Intensität des Ladungstransport-Zustandes detektiert, die auf Grund ihrer wichtigen Rolle in der Trennung von Ladungsträgern, großen Einfluss auf die Leistungsfähigkeit organischer Solarzellen haben. Weitere Untersuchungen zeigten signifikante Änderungen im elektrischen Verhalten. Das Polymer mit geraden und verzweigten Seitenketten ist der vielversprechendste Kandidat für die Herstellung organischer Solarzellen, da es die größten Photoströme liefert. Atomkraftmikroskopie Aufnahmen zeigten unterschiedliche Grade der Phasenseparation zwischen Donor und Akzeptor für die drei Polymere.

Table of Contents

1 Introduction

1.1 Motivation

Since the industrial revolution started in the second half of the 18th century, the world is relying on energy supplies. In figure 1.1 the TPES (total primary energy supply) past and predicted growth between 1850 and 2100 is illustrated. It clearly shows the fast growing demand of energy, especially after the 2nd world war. In the year 2004, 470 EJ (Exa Joule) were estimated as TPES which corresponds to 11.2 gigatons of oil equivalent. A growth of the TPES of about 1.5 to 2% per year is predicted, mostly due to the expected growing overall population. Other reasons are the increased wealth of life and the easy access to consumption. [1]

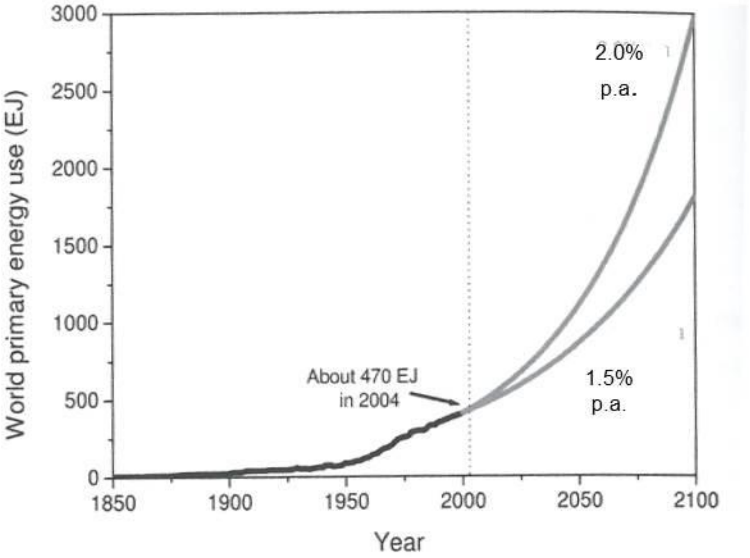

Figure 1.1: *Illustration of the world's total primary energy supply from 1850 to 2100 [1]*

Figure 1.2 shows a diagram of the world's energy consumption sorted by energy source from 2006. It shows that around 86% of the global energy originates from fossil fuels (oil, coal and gas). This energy it not renewable and a major cause for the climate change. [2] Fossil fuels are also limited intrinsically, as the processes of their creation took place over thousands of years ago. [1] 8% of the energy is coming from nuclear power and only 6% are made up from renewable ones. Renewable energy sources include wind, biofuels, geothermal energy and solar energy. As the point of half maximum for oil (point where half of the oil resources on earth are used up) according to predictions is being reached before the year 2025, the production and supply of it will constantly decrease over the years. Also the price will increase dramatically. These facts show the importance of the enhancement of renewable energy sources. [2]

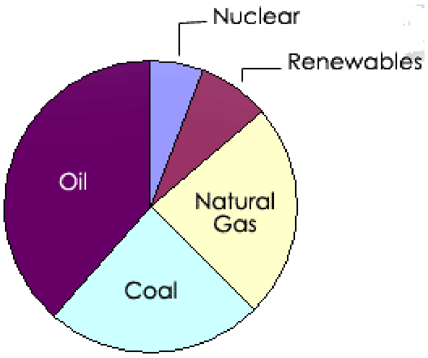

Figure 1.2: *Diagram of the world's energy consumption sorted by energy source for the year 2006 [2]*

A good way to overcome this growing demand of energy is harvesting it directly from sunlight. This is done by using inorganic or organic photovoltaics [3]. Silicon-based solar cells are difficult to produce and expensive as well, [4] but they reach nowadays up to 25.6% power conversion efficiency [5]. For cost and effort reasons, a search for an alternative started. Especially polymer-based solar cells are investigated as low cost alternatives to silicon-based ones for sustainable solar energy conversion. Further advantages of organic devices against silicon-based devices are: low weight, flexibility of the thin layers [1], and solution processability [3]. Over the past 29 years the conversion yield of solar cells based on organic materials increased significantly. While 1% in 1985 [6] and 5% in 2000 were achieved [7], in 2014 power conversion efficiencies up to 10.7 % are reached [5]. Therefore organic photovoltaics seem to be a reasonable topic for research. It is expected to become a source of terawatt energy. [1]

1.2 Organic photovoltaics

1.2.1 Conjugated polymers and fullerene derivatives

In general, a polymer can be regarded as a large molecule (macromolecule). This macromolecule consists of a large number of repetitions of subunits (monomers) that are linked together covalently. If only one type of repeat unit forms these molecules, they are called homopolymers. Molecules which consist of more than one type of repeat unit are called copolymers. [8] Polymers with repetition units only arranged in one dimension are called linear polymers, they have only one main chain as the polymer backbone.

In figure 1.3 a) the commonly used polyethylene is illustrated as an example for polymers which have only single bonds is their main chain. These bonds create σ-orbitals, which result in a cylinder symmetric distribution of the electrons. Polymers which only possess σ-orbitals are in general colourless and are acting as insulators. Therefore they do not have mobile charge carriers and cannot be used in organic electronics. Figure 1.3 b) shows polyacetylene as an example for another type of polymer. This one has alternating single and double bonds between the carbon atoms in their main chain.

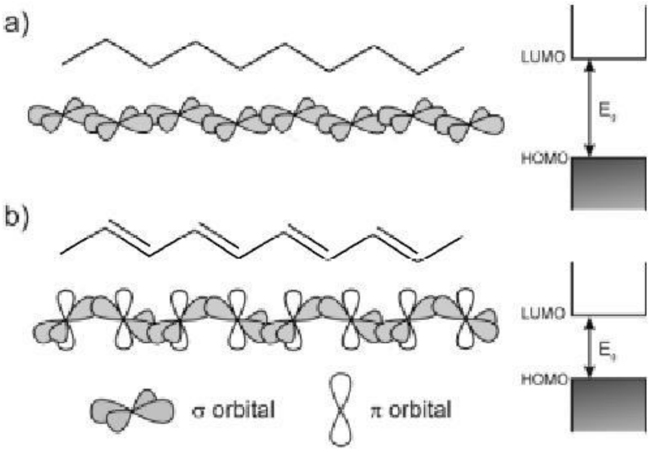

Figure 1.3: *Illustration of a polymer with single bonds (a) and a conjugated polymer (b [9]*

This configuration leads to the formation of particular molecular orbitals. Two σ-bonds are formed due to sp^2-hybridization and a π-bond that comes from an overlap of atomic p_z-orbitals. The latter is orientated perpendicular to the horizontal plane of the polymer backbone. Thereby π-orbitals are formed above and below the polymer's horizontal plane. Due to the overlap (conjugation) of the π-orbitals, electrons are delocalized along the conjugation and an energy-band-like structure is formed (illustrated on the right side of figure 1.3). The highest occupied molecular orbital (HOMO) is separated by a band gap from the lowest unoccupied molecular orbital (LUMO). Polymers with these properties are called conjugated polymers. They are semiconductors or even conductors (condition: enough charge carriers are available intrinsically or by doping). Conjugated polymers are called optically active, if the excitation energies to lift an electron from the HOMO to the LUMO level are in the visible wavelength range. [9]

Fullerenes belong to the class of conjugated small molecules (to distinguish from macromolecules, as e.g. polymers). Since the discovery of the Buckminster fullerene C_{60} in the 1980's by Kroto et al. [10], they have attracted attention in different fields of science, like chemistry, biology and physics. Fullerenes itself are all carbon allotropes and have a spherical shape (also called carbon cage) composed of hexagonal and pentagonal carbon rings. Fullerenes can be viewed as large, three dimensional π-electron systems. [11] Examples for basic fullerenes are C_{60}, C_{70} and C_{84}. The C_{60} molecule is shown in figure 1.4 on the left. It is composed of 60 carbon atoms, which are arranged in 12 pentagonal and 20 hexagonal rings and showing a soccer ball-like structure. [12] The absorption spectra of C_{60} and C_{70} show weak absorption in a range between 430 nm and 620 nm that might arise from a forbidden transition. Stronger absorption peaks appear at smaller wavelength in the UV region. [13] By attaching different side groups to the fullerenes, their properties for various applications can be tailored additional to the basic properties of the fullerene. The most common fullerene derivative used in polymer electronics and photovoltaics is [6,6]-phenyl-C_{61}-butyric acid methyl ester (PCBM). Its structure is illustrated in figure 1.4 on the right. [12]

Fullerenes and their derivatives have a high electron affinity and a high electron mobility, therefore they are widely used as acceptors in organic solar cells. [14]

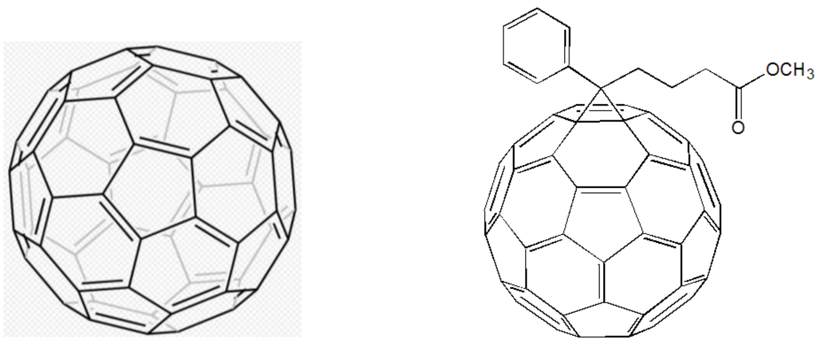

Figure 1.4: *Illustration of the chemical structure of the fullerene* C_{60} *(left) [22] and the fullerene derivative* $PC_{70}BM$ *(right) [12]*

1.2.2 Types of organic solar cells and working principles

A main difference between organic and inorganic solar cells is the strong localization of the excitons (Frenkel-excitons) generated by incident sunlight and the high binding energy of electron-hole pairs that are eventually obtained by charge transfer at the donor/acceptor (D/A) junction. Reason for the strong localization of the excitons in organic semiconductors is mainly molecular disorder. In most cases the exciton is generated and remains on one molecule. Only in perfectly ordered systems the exciton can be transferred between different molecules by energy transfer (Förster transfer). The high binding energy of the electrons is a result of the low dielectric constant of organic semiconductors. Low dielectric constant means that screening of electric fields in the material is low, therefore the Coulomb attraction between opposite charges are strong. This energy is much smaller in inorganic semiconductors because they have a high dielectric constant and because of that fact free charge carriers can be created under ambient conditions immediately by excitation across the band gap. In organic semiconducting materials first localized excitons are formed instead of free charge carriers. Therefore organic solar cells need an additional mechanism to dissociate these first into bound charge pairs. This dissociation takes place at the donor/acceptor interface. This interface is formed between two organic materials with a sufficient difference in energy of the HOMO and LUMO energy levels, respectively. This energy offset has to be large enough to make the charge transfer energetically favourable compared to the excited state (usually >0.4 eV). As this charge transfer (CT) state is still localized at the interface, a further mechanism is needed to separate the charges. This is achieved by an electric field across the device, provided by the work function difference of the electrodes of the solar cell. At that stage, the charge separated (CS) state, the charges are finally free and can move to their respective electrodes.

Typical materials used in organic photovoltaic are conjugated polymers and fullerene derivatives. In such devices the polymer acts as electron donor material, which has the lower ionization potential and the fullerene derivative acts as electron acceptor, which has the higher electron affinity. [1]

An illustration of two different device architectures is shown in figure 1.5. One electrode has to be transparent in order to make light absorption in the active layer possible. Indium tin oxide (ITO) is commonly used as the transparent electrode in organic photovoltaics. ITO is a mixed oxide and consists of 90% In_2O_3 and 10% SnO_2. [15] The electron donor is shown in green and the electron acceptor material in red in the illustrations. The thickness of the active layer should be around 100 nm. Typically used materials for the cathode are aluminium or silver as they have a lower work function compared to ITO and are able to reflect the not absorbed photons back into the active layer. ETL and HTL are electron and hole transport layers, which are used to make sure that only holes are reaching the anode and only electrons are reaching the cathode. A typical material for a hole transport layer is poly(3,4-ethylenedioxythiophene):poly(styrenesulfonate) (PEDOT:PSS). PEDOT is a conjugated polymer doped with PSS and was invented in the 1980's. [15] In organic solar cells, a PEDOT:PSS layer with a thickness of less than 100 nm is sandwiched between the ITO electrode and the active layer. This is done to pin the ITO's high work function (5.2 eV) after O_2-plasma-activation, to smooth the rough surface of ITO (to avoid short circuits) and to protect the active layer from diffusion of indium or oxygen. [16] As ETL commonly a layer of lithium fluoride with a thickness of around 1 nm is used. [17]

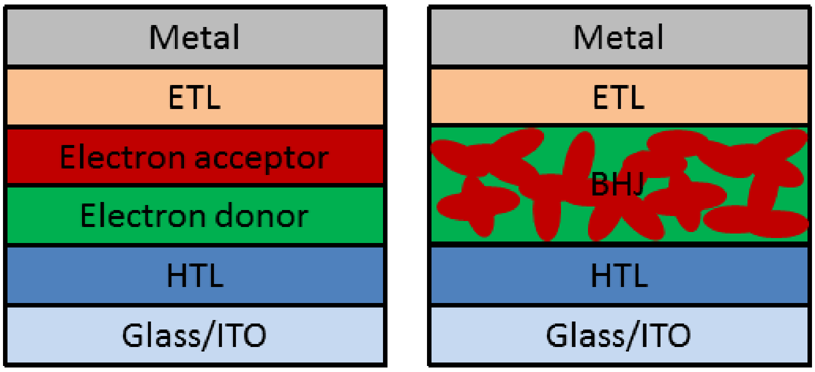

Figure 1.5: *Schematic illustration of a bilayer solar cell (left) and a BHJ solar cell (right) (adapted from [21])*

In a bilayer device, the donor layer is formed on top of the acceptor layer, where in a bulk heterojunction (BHJ) device donor and acceptor materials are mixed with each other.

As mentioned, the process of photoinduced charge carrier generation in organic solar cells includes several steps. A general scheme summarizing the most important mechanisms involved in charge generation in an organic solar cell is illustrated in figure 1.6. These are in detail:

1. Photon absorption: Only those photons get absorbed, which have an energy equal or higher than the band gap energy (E_g) of the organic semiconductor. The excess energy of photons higher than E_g is transferred to the molecule environment as phonons (molecule vibrations). This is called thermalization.
2. Exciton generation: In the general picture, an electron is lifted from the semiconductor HOMO to the LUMO level by absorption of the photon energy. However, for a disordered organic it is more precise to refer to molecular levels, in which the electron is lifted from the ground state S_0 to the excited state S_1 (S stands for singlet and is a quantum mechanical state with paired spins). This process is called photoexcitation. Due to disorder, the excited state is localized to the molecule. These kind of short-range excitons are called Frenkel-excitons. It has a distinct, finite lifetime of ~1 ns.
3. Diffusion of excitons: the created exciton is not carrying any net mass or charge. It diffuses through the donor material by Förster (long range) or Dexter transfer (short range). Förster transfer is basically an energy transfer process, which can be imagined like a emission/absorption transfer between molecules. During Dexter transfer basically charge pairs are transferred from one molecule to the other. This is limited to adjacent molecules. Both processes only take place as long as there are no competing decay pathways present.
4. Dissociation of excitons: This step takes places at the donor acceptor interface. To dissociate the exciton, a high local electric field is required. The electric field provided by different electrode work-functions is too weak for that. The difference in electron affinities (and ionization potentials) between donor and acceptor material at the D/A interface is large enough to make a charge transfer across the interface (meaning from a donor to an acceptor molecule) energetically favourable. Result is a charge transfer (CT) state at

the interface, with a hole on the donor molecule and the excited electron on the acceptor molecule. They are still bound by Coulomb attraction.

5. Charge separation: To overcome the Coulomb attraction between the hole and the electron at the interface (typically ~0.4 eV, due to the lack of screening in low dielectric constant material), an electric field across the device is required. This driving force has to be provided by the work-function difference between the anode and cathode.
6. Transport of charge carriers towards the electrodes: Electrons are moving through the acceptor and holes through the donor by hopping transport. Charge mobilities in organic semiconductors are generally much lower than in inorganic ones and traps can reduce the mobility of the charge carriers additionally.
7. Charge collection at the electrodes: To make this step most efficient, the Fermi energy of the cathode must be smaller than the LUMO energy of the acceptor and the Fermi energy of the anode must be larger than the HOMO energy of the donor. [18] [19]

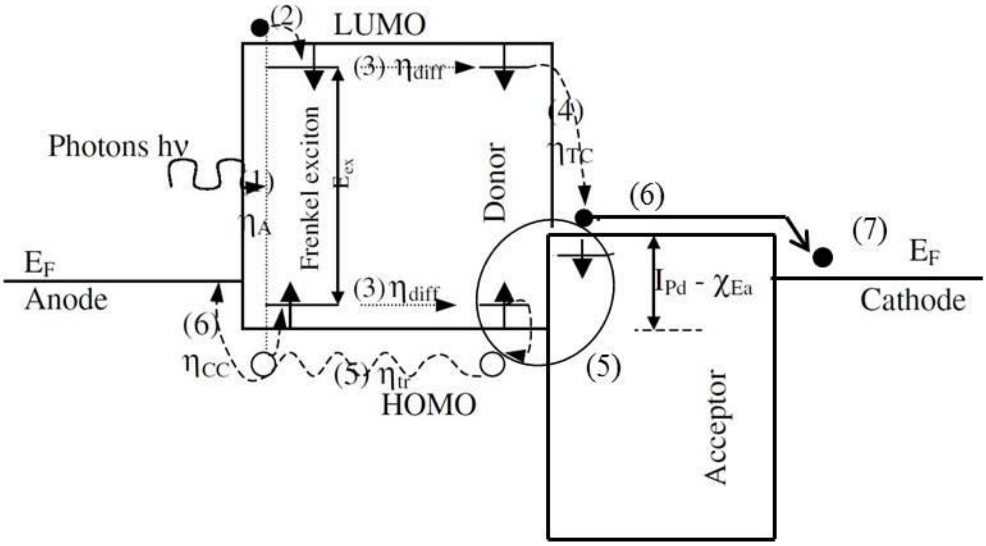

Figure 1.5: *Schematic illustration of a bilayer solar cell (left) and a BHJ solar cell (right), adapted from [18]*

The big advantage of BHJ devices is the larger interface area of donor and acceptor phase compared to bilayer devices. This is due to the intimately mix of the two components in a bulk volume. That means that more efficient exciton dissociation is possible, because the D/A interfaces are within less than the exciton diffusion length of about 10 nm, when the phase separation of donor and acceptor are optimized. [20]

These dispersed interfaces throughout the whole bulk should make sure that there are no losses due to too small diffusion length of the excitons. Also recombination should be reduced, because the charges are separated within their respective phases. For contacting the electrodes selectively, percolated pathways for both phases are necessary to transport electrons and holes there. Hence, nanomorphology plays an important role in BHJ devices. It can be influenced by thermal annealing of the solar cells. Where the chemical structure of donor and acceptor material is determined by the solubility in the solvent and their miscibility, thermal annealing causes recrystallization and also reduces the density and free volume of defects which appear at the interfaces. [21] [22]

2 Materials

In this section the polymer F8T2 and its derivatives with different ordered side chains and ICBA is introduced. The synthesis route of the polymer is shown and important properties of both materials are summarized. Further an illustration of the energy levels of the materials can be found in this section.

2.1 F8T2 derivatives with varying side chains

Poly[(9,9-dioctylfluorenyl-2,7-diyl)-*co*-bithiophene] (F8T2) is a conjugated copolymer with alternating dioctylfluorene and bithiophene monomer units incorporated into the main chain. This polymer is acting as an electron donor in organic solar cells. It is attractive for the fabrication of photovoltaic devices, because of its high charge carrier mobility and broad absorption in the visible range.

In this thesis three different types of F8T2 were investigated according to performance differences in solar cells: F8T2 with straight octylchains (P1), F8T2 with branched 2-ethylhexyl side chains (P2) and finally a derivative with a mixture of both types of side chains (P3). In figure 2.1 (top row) the chemical structures of the three different types of this co-polymer are illustrated. The glass transition temperatures (T_g) are 110°C for P1, 113°C for P2 and 111°C for P3, respectively. The molecular weights and the polydispersity (PDI) of the three polymers can be found in table 2.1. Induced by altered side-chain structure, different stacking behaviour upon crystallization of the polymers can be expected. A suggested possible stacking structure of the three polymers is shown in figure 2.1 (bottom row). [23] Thereby P1 might have the smallest stacking distance, because the non-bulky straight octylchains allow interdigitation ("zipper-like" structure) of the side-chains during main-chain stacking. The bulky branched side chains of P2 on the other hand do not permit this, suggesting end-to-end (of the side-chain) stacking and in consequence a stacking distance of twice the side-chain dimension. For P3 with the mixed side chains, the stacking distance might be further increased compared to P2. This is a result of the combination of the more bulky branched side chain (preventing interdigitation) and the longer straight side chain, enforcing end-to-end stacking in the distance of the twice the octyl chain dimension. Where P1 should have the highest ability to crystalize, this tendency should be reduced in P2 and P3 by increasing the stacking distances and therefor lead to a more amorphous polymer. Their molecular weights are listed in table 1, where can be seen that P1 has a significantly higher molecular weight than P2 and P3.

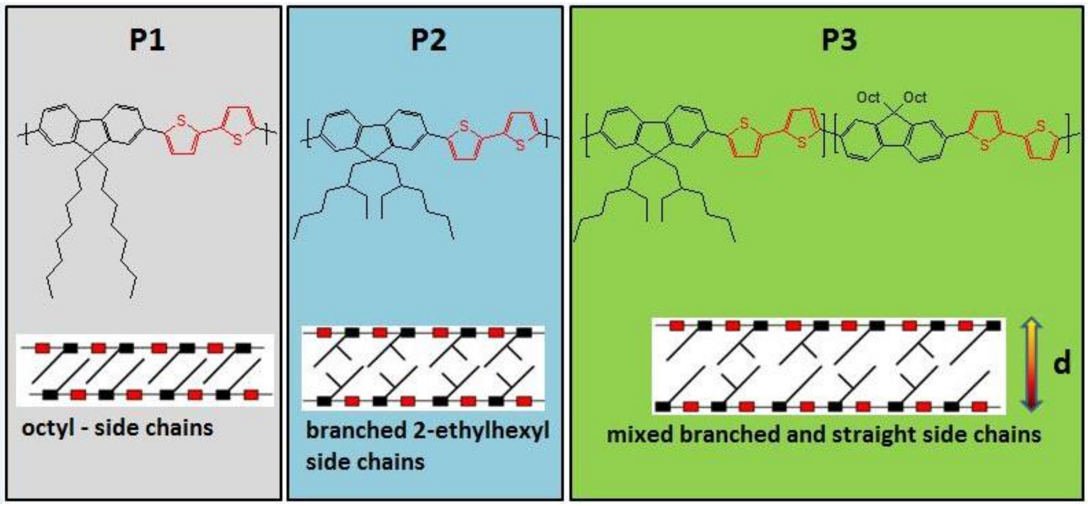

Figure 2.1: *Chemical structures (top row) and possible stacking structures (bottom row) of the three investigated polymers, adapted from [23]*

Table 2.1: *Molecular weight and polydispersity of the F8T2's*

	P1	**P2**	**P3**
M_n [g/mol]	29700	13300	10850
M_w [g/mol]	140700	23400	32250
PDI	4.73	1.77	2.97

The polymers have been synthesized by Suzuki polycondensation during the PhD thesis of Andreas Pein [23]. Suzuki polycondendation uses palladium-based coupling between monomers that contain halide groups and monomers that contain organoboron groups. [24] The synthesis schemes are depicted in figure 2.2 (top row) for the polymers P1 and P2 and in the bottom row for P3. According to several publications, like for example Huang et al. [25], the best performances of F8T2:PCBM solar cells are observed by using an annealing temperature of 70°C. At higher annealing temperatures, that are closer to its glass-transition temperature (T_g) of 130°C, the polymer favours the formation of bulky clusters. As a consequence of the enormous distance to the D/A interface in this case, the performance of the solar cells decreases significantly, as many generated excitons decay before reaching the interface. For D/A systems like the present one, where the phase formation is influenced by annealing, low temperatures lead to poor device performance as well.

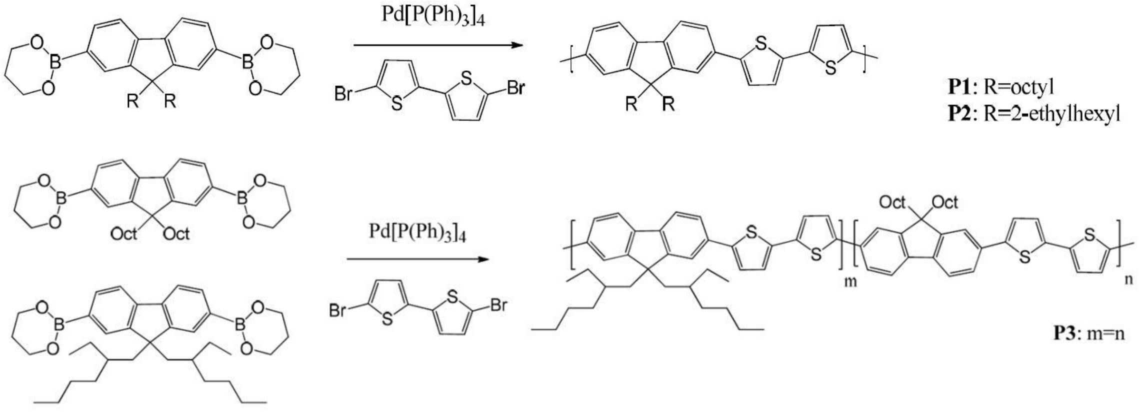

Figure 2.2: *Synthesis scheme for P1, P2 (top row) and P3 (bottom row)[23]*

2.2 ICBA

Indene-C_{60} bisadduct (ICBA) is a fullerene derivative, which is quite attractive for use as acceptor in organic solar cells. This is due to its higher lying LUMO energy of ICBA (-3.74 eV) compared to the commonly used [6,6]-phenyl-C_{61}-butyric acid methyl ester (PCBM) (-3.91 eV). An Illustration of the chemical structure is shown in figure 2.3.

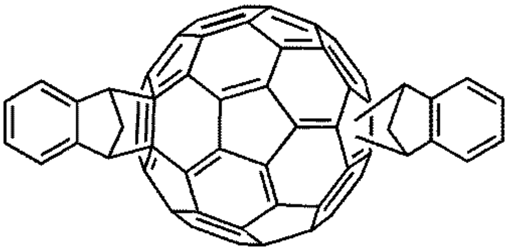

Figure 2.3: *Illustration of the chemical structure of ICBA [37]*

2.3 Energy levels

In figure 2.4 an energy level diagram of F8T2, $IC_{60}BA$ and $PC_{70}BM$ is given. F8T2 has a HOMO energy of -5.41 eV and LUMO energy level of -2.48 eV. [23] The HOMO and LUMO levels for the two acceptor materials are -5.87 eV and -3.91 eV for $PC_{70}BM$ and -6.10 eV and -3.74 eV for $IC_{60}BA$, respectively. $PC_{70}BM$ is nowadays one of the most commonly used acceptor materials is organic photovoltaics, due to absorption in the red wavelength range. The maximum value of the open circuit voltage is determined by the cross-band gap energy, which is the energy difference between the HOMO level of the donor material and the LUMO level of the acceptor material minus the voltage losses at the electrodes. [26] As the illustration shows, ICBA has a higher lying LUMO level than $PC_{70}BM$, which makes it an attractive acceptor material, due to the predicted higher efficiencies due to the higher open circuit voltage.

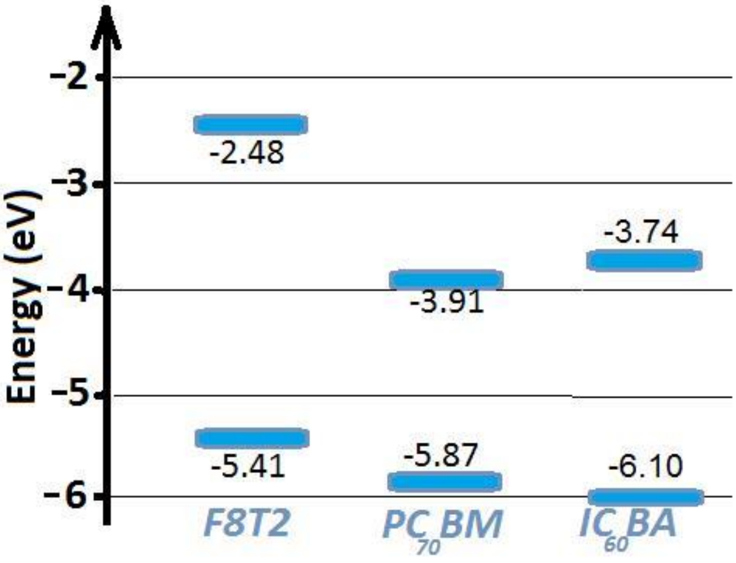

Figure 2.4: *Energy level diagram of F8T2, $PC_{70}BM$ and $IC_{60}BA$*

3 Analytical methods

3.1 Electrical characterization

3.1.1 I-V Characterization

The three electrical parameters, which characterize an organic solar cell, are the open circuit voltage (V_{OC}), the short circuit current density (J_{SC}) and the fill factor (*FF*). All of these parameters can be derived from current-voltage curves. Examples for I-V characteristics of a solar cell in the dark and under illumination are shown in figure 3.1. The illustration on the left-hand side is plotted linearly on the y-axis (which is the current density) and the one on the right in logarithmic scale. It can be seen that in the dark almost no current flows, until the contacts are starting to inject charge carriers. This happens for voltages that are larger than the open circuit voltage. Under illumination, power is generated, as can be seen in the fourth quadrant between short circuit current and open circuit voltage. The maximum power point (*MPP*) highlights the point where the product of voltage and current are the largest. The fill factor (*FF*) gives information about the shape of the current-voltage curve:

$$\mathrm{FF} = \frac{\mathrm{J_{mpp}} * \mathrm{V_{mpp}}}{\mathrm{J_{sc}} * \mathrm{V_{oc}}} \tag{1}$$

The total power conversion efficiency can be calculated via:

$$\eta = \frac{\mathrm{J_{sc}} * \mathrm{V_{oc}} * \mathrm{FF}}{\mathrm{P_{in}}} * 100\% \tag{2}$$

J_{mpp} and V_{mpp} are the current density and the voltage at the maximum power point. P_{in} is the incident light power density, which is standardized at 1000 $\mathrm{W/m^2}$. This is in accordance to the AM 1.5 G standards and its spectral intensity distribution corresponds to that of the sun on the earth surface at an incident angle of 48.21°. [22]

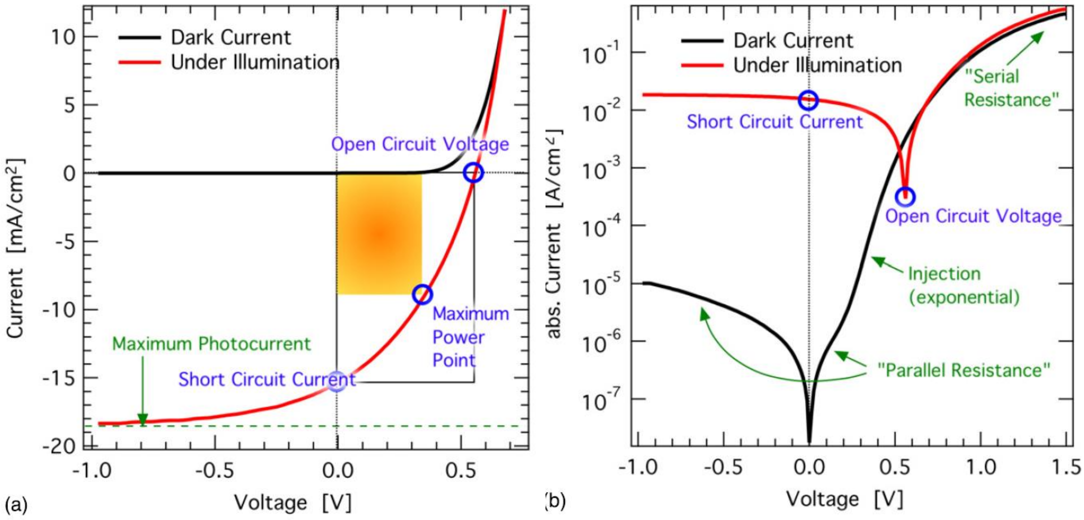

Figure 3.1: *Schematic illustration of IV-curves in the dark and under illumination plotted linear (left) and semi-logarithmic (right) [22]*

Open Circuit Voltage: In a bulk heterojunction solar cell the maximum available voltage is determined by the offset between the HOMO level of the donor material and the LUMO level of the acceptor material. V_{OC} is lowered from this value by charge carrier losses of about 0.2 eV at each electrode. [26] Another impact is the nanomorphology of the active layer. To provide a better match between the energy levels of hole collection electrode (ITO anode) and the HOMO of the of the hole conducting material the work function of the anode can be modified by O_2 plasma etching or coating with an organic hole transport layer with a higher work function (PEDOT:PSS). Effects at the interfaces between the metal and the organic materials, like for example oxide formation, can change the work function of the metal and so take influence on the open circuit voltage, too. In general, V_{OC} is a very sensitive parameter that strongly depends on the energy levels of the used materials and their formed interfaces. [22]

Short Circuit Current: The short circuit current density is a direct measure for the efficiency of charge generation and separation, scaling with the area where this processes take place. [1] Considering ideal and loss free contacts, J_{SC} follows the following formula:

$$J_{SC} = ne\mu E \tag{3}$$

That means that J_{SC} is determined by the photoinduced charge carrier density and the mobility μ of the charge carriers within the device. Thereby n is the charge carrier density, which would be the number of photons absorbed per unit volume, assuming 100% efficiency for charge carrier generation. Further, E is the electric field and e is the elementary charge. The difficult thing about the mobility of the charge carriers in organic solar cells is that μ is not solely a material parameter, but rather a device parameter. It is strongly influenced by the nanoscale morphology of the thin film, which is hard to control in BHJ devices and highly anisotrop.

Fill Factor: This value is determined by the charge carriers that are reaching the electrodes, when the built-in field is lowered towards V_{OC} . In an ideal solar cell the fill factor would reach 100%. In a real organic solar cell it is affected by the competition between charge carrier recombination and transport and reaches usually 30-65 %. [22]

Loss mechanisms in organic solar cells can be described with equivalent circuit diagrams, like the one that is illustrated in figure 3.2. J_{SC} is the short circuit current and J_{dark} is the dark current. In general the loss mechanisms can be separated in series resistance (R_s) and shunt resistance (R_{sh}). R_s is related to losses due to low mobilities, contact- or interface resistance or trapping. Thus this value should be minimized. The shunt resistance is related to leakage processes. [27] To get a high FF the parallel shunt resistance should have a large value to prevent leakage currents and R_s should have a low value to get a sharp rise in the forward current. [21]

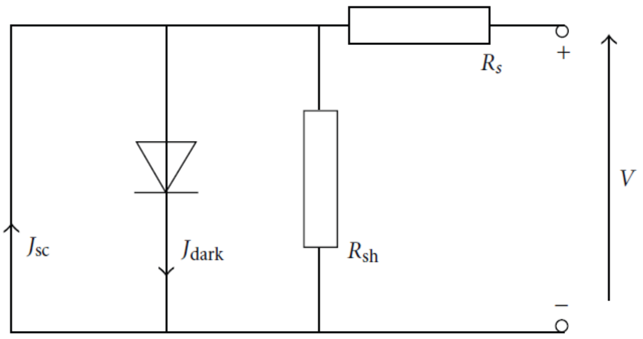

***Figure 3.2:** Equivalent circuit diagram for an organic solar cell [27]*

3.1.2 Spectral Response

Another measure for the device performance is the spectral response. It is defined by the external quantum efficiency (EQE) over the incident wavelength. It follows the formula:

$$EQE(\lambda) = \frac{1240 * J_{sc}(\lambda)}{\lambda * P_{in}(\lambda)} \tag{4}$$

Here $J_{SC}(\lambda)$ is the short circuit current density at a certain wavelength, $P_{in}(\lambda)$ is the incident power at a certain wavelength and λ is the wavelength. It is derived by the number of collected electrons divided by the number of incident photons at a particular irradiation wavelength times the wavelength multiplied by a constant factor. [22] This value gives information about the conversion efficiency of all incident photons to electrons at a certain irradiation wavelength. In contrast to the internal quantum efficiency (*IQE*), where only photons are counted that are absorbed by the active layer, so reflected or scattered electrons are not taken in account. [1] In figure 3.3 [28] the difference between internal and external quantum efficiency is illustrated for a silicon solar cell. Where the *IQE* has a broad range with efficiencies up to 100%, the behaviour of the *EQE* curve shows losses. Also the surface reflectance depending on the wavelength is shown.

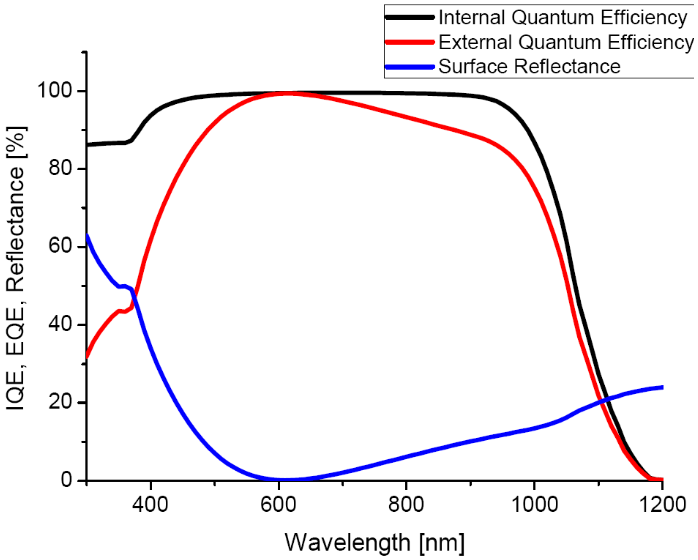

Figure 3.3: *Schematic illustration of the EQE, IQE and surface reflectance [28]*

3.1.3 Electroluminescence

Electroluminescence (EL) is a process, where light is emitted due to an applied forward voltage bias to a diode. Thus it is the inverse to the photovoltaic effect that takes place in solar cells, where incident light is converted into an electrical current. Applying a forward bias to an organic solar cell causes injection of opposite charge carriers into the semiconductor, promoting their radiative recombination. Not all of them will recombine radiative, due to solar cells materials not being good emitters in general. Part of them will recombine nonradiatively, by generation and decay of triplet excitons (75% by definition) or by phonons. The emission of the radiative part of the recombination can be detected and shows energies around the bandgap of the different materials and also the energy of charge transfer states, which have energies below the one of the bandgap. There are two common ways to perform EL imaging. The first one uses spectrally resolved measurements as function of temperature or injection current. The other possibility is imaging with a charge-coupled device (CCD camera, where spatially resolved information can be obtained by measuring durations of the EL emission). Two different set-ups for EL measurements are illustrated in figure 3.4. On the left, a setup for spatially resolved measurements can be seen. It consists of a CCD camera, a power supply unit and a PC. The measurements are performed in a dark chamber to protect the samples from ambient light. The setup on the right is used for spectroscopic investigations. It consists of a monochromator, a Germanium detector or photomultiplier (depends on the required sensitivity) and a lock-in amplifier.

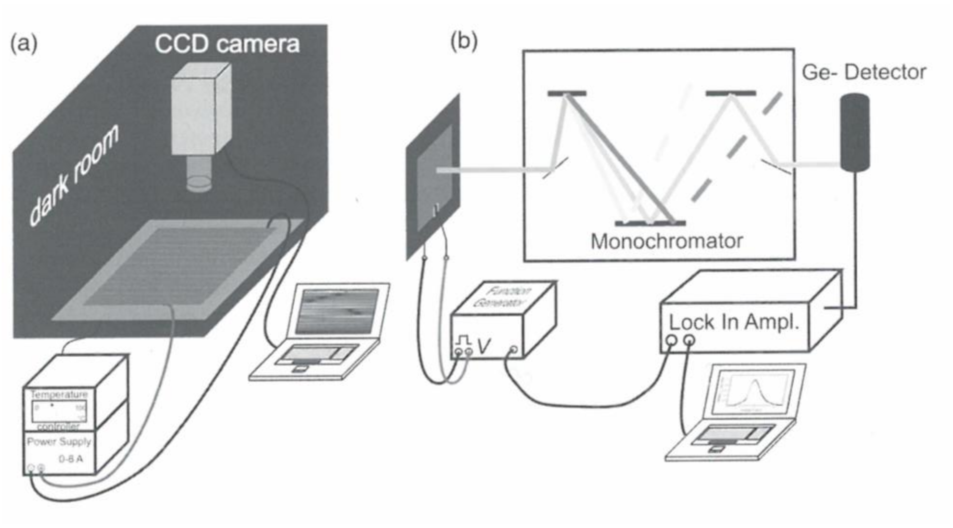

Figure 3.4: *EL set-ups for spatially resolved measurements (left) and for spectroscopic investigations [29]*

Spectrally resolved EL measurements are rarely used for the characterization of solar cells, even though it is related to quantum efficiency measurements. This is due to the fact that there are more sensitive methods available, like photoluminescence (PL) measurements. [29]

3.2 Photophysical characterization

3.2.1 Photoluminescence

In organic semiconductors an excited singlet state S_1 is populated by illumination (generation of an exciton). After a certain lifetime that state may decay back to the ground state S_0. There are different processes how excited molecules can go back to the ground state. The process, where light is emitted directly from the $S_1 \rightarrow S_0$ decay (lifetime ~ns), is called fluorescence. Also non-radiative decay is possible, which happens by phonons. Alternatively, the excited state might undergo intersystem crossing (ISC) to a triplet excited state $S_1 \rightarrow T_1$. Triplets are quantum mechanical states with unpaired spins. The probability of an excited state for ISC is increased if their vibrational levels overlap. A triplet exciton will also decay to the ground state after a certain lifetime. Since the decay $T_1 \rightarrow S_0$ is actually spin-forbidden, its rates are much lower than for singlet decay. The resulting emission has therefore a considerably longer lifetime (~µs-ms) and is called phosphorescence. Also decaying CT-states and recombining charges (polaron emission) can be emissive, with intermediate lifetimes (ns-µs). Other processes that might appear are intermolecular charge transfer and excited state interactions with other molecules. All of these interactions can be seen in a photoluminescence spectrum. [11] Photoluminescence quenching is a desired process in an organic solar cell, because it shows that the formed excited states are successfully dissociated and charges are separated before decaying radiatively. Quenching means in this case, that the PL intensity of the sole photoactive material is strongly decreased in the D/A blend. If a blend shows quenching and the device nevertheless shows poor performance, this might be related to non-radiative decay processes or related to charge transport/collection issues of the device. [1]

3.2.2 Time correlated single photon counting

Time correlated single photon counting (TCSPC), also called single photon timing technique (SPT), is a technique to measure the fluorescence decay lifetime of excited states. This technique belongs to the pulse fluorimetry methods, where short light pulses are used to excite the sample and delta–pulses are detected as response. The choice of the light source depends on the desired excitation wavelength. Flash lamps for example work in a wavelength range that is limited from 200 to 400 nm and generate nanosecond pulses. Solid state lasers are a more preferable choice, because they are working in a wavelength range from 680 to 1100nm and generate pulses with width between some tens of femtoseconds to around 100 picoseconds. To get excitation wavelength in the visible and UV regions, frequency doublers and triplers can be used.

The working principle of TCSPC is as follows: the sample gets excited by a light pulse and the fluorescence intensity can be detected. This intensity at the time t is proportional to the probability of detecting a single photon at the same time t. In this way fluorescence intensity decay curves can be recorded by recording single photons following exciting pulses.

A schematic illustration of the TCSPC set up is shown in figure 3.5. First an electrical pulse, which is associated with the optical one, is generated and forwarded through a discrimination unit to start the time-to-amplitude converter. At the same time the sample gets irradiated by the optical pulse to generate fluorescence emission. For each excitation pulse only one photon can be detected by the photomultiplier. The electrical pulse, which corresponds to that signal goes through a discriminator and gives the stop signal to the time-to-amplitude converter. This converter gives the output pulse. The delay time between the starting and stopping pulse is directly proportional to the amplitude of the output pulse. The heights of the pulses can be analysed by using an analog-to-digital converter and a multichannel analyser. To build up a pulse height histogram as shown on the bottom of the illustration, a large number of excitation and detection events have to take place. It shows the decay curve where the accuracy depends on the delta-pulse response of the system. [11]

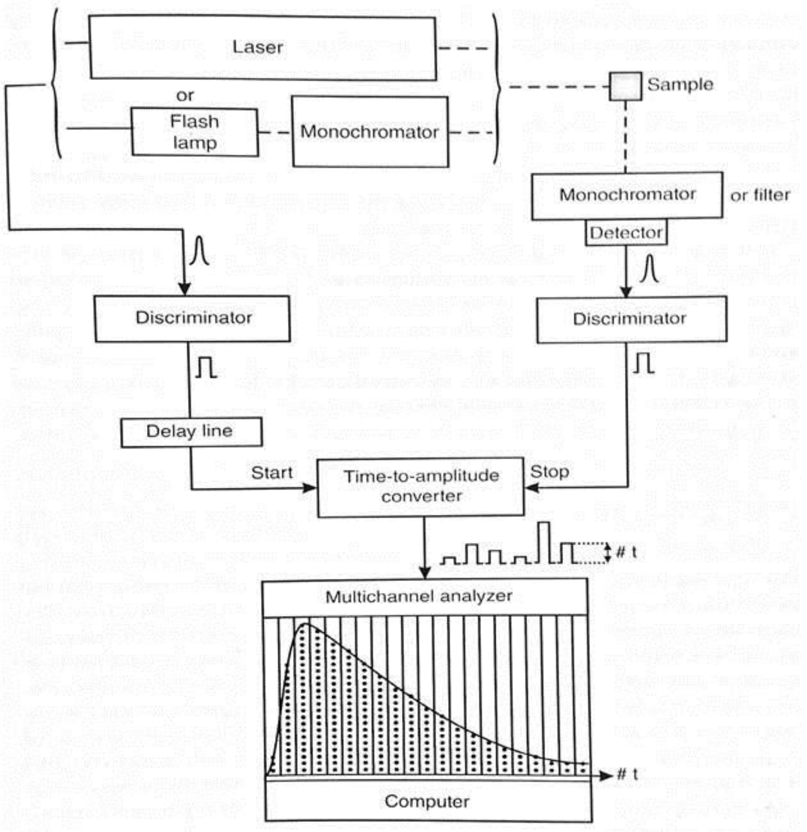

Figure 3.5: *Schematic illustration of the set-up for TCSPC measurements [11]*

3.2.3 UV-VIS Absorption

To investigate the optical absorption profile of the fabricated blends in the visible and ultraviolet wavelength range, UV-VIS absorption spectroscopy is used. Absorbance is, according to Lambert-Beer’s Law, directly proportional to the thickness of the layer and the concentration of the absorbing species.

If the energy of the photons that irradiate the sample is the same as the energy difference of two electronic states, electrons can be excited to a higher energy level by absorbing these photons.[30] The structure of absorption spectra follows not only electronic excitations, but also vibrational ones, which is particularly pronounced in organic materials. The condition for both of these excitations is that they only take place if the molecular structure is changed by transferring the electron to a higher energy level. The Franck-Condon principle is illustrated is figure 3.6. According to that principle, electronic transitions are taking place much faster than the motions of the atomic nuclei of a molecular skeleton. That’s why they are only occurring at constant positions of the nuclei. This is illustrated in the drawings by vertical arrows that start at the vibrational ground state $n_v = 0$ in the electronic ground state S_0. The upper left figure shows a structure that’s not affected by electronic excitation (meaning position of the nuclei is the same for the ground and the excited state). Therefore the vertical transition leads from the electronic ground state S_0 to the vibronic ground state S_1, as the most probable excitation. For an excitation like that, the spectrum only consists of one sharp absorption peak (top, right). The illustration on the bottom left shows what happens when the molecule exitation changes the position of the nuclei compared to the molecule in the ground state (e.g. some molecules show extended bond length upon excitation). This causes a shift of the nuclear coordinate X. Since the excitation still goes vertically, electronic excitation gets coupled to an excitation of a vibronical state. The arrow starts here in the vibration ground state of the electrical ground state and ends in an excited vibrational state of the electrical excited state S_1. The spectrum that belongs to that transition shows a distinct fine structure, what can be seen on the bottom right. Another property that can be evaluated from the spectra is a red shift because of differences in the molecular weight of the used polymers. [31]

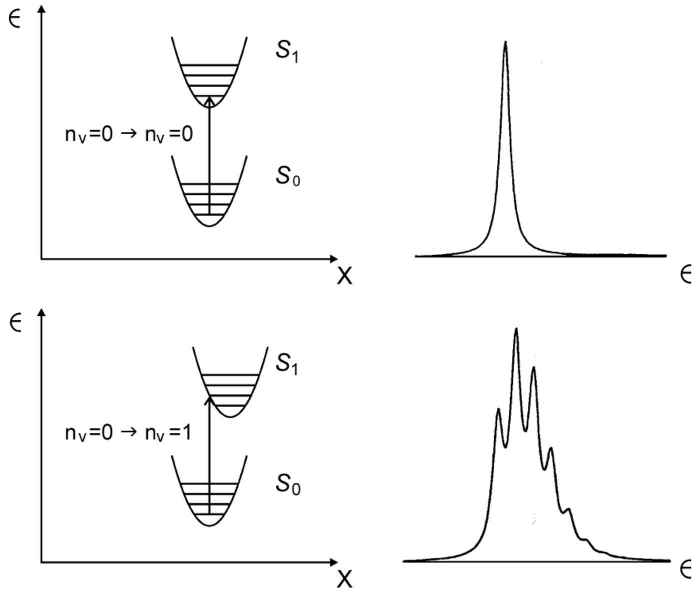

Figure 3.6: *Illustration of the Franck-Condon principle [31]*

3.3 Morphological Characterization

3.3.1 Atomic Force Microscopy

Atomic force microscopy (AFM) is a popular tool to investigate the surface morphology of films. It consists of a flexible cantilever with a sharp tip on one end. This tip should consist of a single atom at the end to provide best resolution. Typical materials for tips are Si compounds or diamond, because they should not deform when hitting the sample. The cantilever is moved across the sample surface, which causes deflections that are usually detected by a laser beam that gets reflected off the back of the cantilever into a photodiode detector. When the sample and the tip are close enough the each other, 4 different forces are present, that influence the motion of the cantilever and give information about the surface:

- An attractive force due to van der Waals interactions, that occurs for distances larger than 4 Å.
- A short range force, which occurs because of tunnelling of electrons between sample and tip. It is repulsive, due to the Pauli exclusion principle.
- Capillary forces, that occurs when measuring on air, because of condensation of water on the sample surface.
- Coulomb forces, those are long ranged and arise from electrostatic charging effects.

An AFM can be used in three different modes: contact mode, noncontact mode and tapping mode. The most common one to investigate organic blends is the tapping mode. Here the cantilever oscillates at its resonance frequency across the sample and the tip lightly taps on the surface. When the tip gets close to the sample surface, the electrostatic forces increase, which decreases the measured oscillation of the cantilever. A feedback loop provides a constant oscillation amplitude by moving the scanner vertically at every x, y data point. By recording this movement a topographical image is formed. [32] [33] The principal set up of an AFM is shown in figure 3.7.

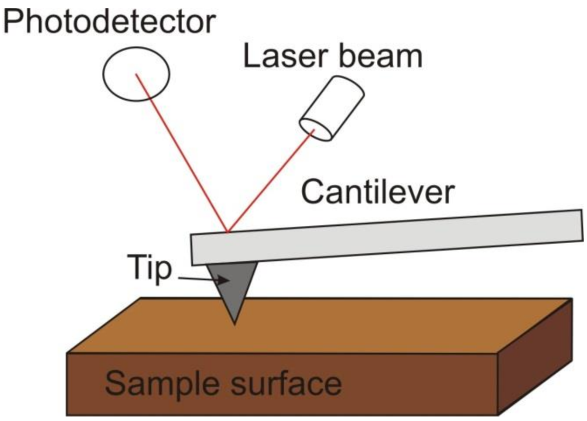

Figure 3.7: *Schematic set-up of an AFM [33]*

3.3.2 Grazing Incidence X-Ray Diffraction

In-plane grazing incidence X-ray diffraction (GIXRD) is an extensively used method in surface science to investigate thin films. The crystallinity and crystal orientation of surfaces can be studied by this technique. [34] It is favoured for the investigation of thin films, compared to other diffraction methods, because of the much better signal-to-background ratio. [35] GIXRD uses the limited penetration depth of evanescent waves that appear when the incident X-rays get totally reflected at the grazing angle to the surface. Because of the reflected waves only penetrating a few nanometres in the material, when measurements are performed below the grazing angle, this method is very surface sensitive. [34] Figure 3.8 shows a schematic illustration of GIXRD. For performing this measurement a synchrotron source is required. The incident beam is labelled by k_i and the angle α_i is below the critical angle. The diffracted one is labelled by k_f with the angle α_f. Depending on the order of the system, different Bragg-like reflections can be obtained. [36]

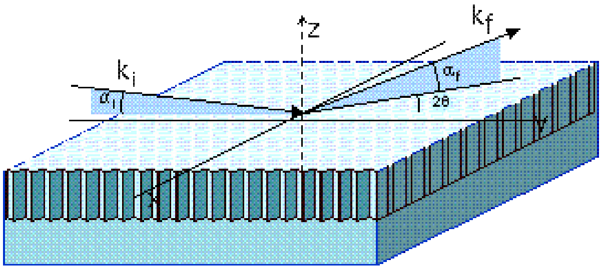

Figure 3.8: *Schematic illustration of GIXRD [36]*

4 Experimental

4.1 Device fabrication

The ICBA used in this thesis was purchased from Ossila Ltd. with >99% purity. [37] The F8T2 was synthesized in-house by Pein et al. [23]. Further information about the properties of the used material can be found in chapter 2. The PEDOT:PSS formulation PEDOT:PSS Clevios P Jet OLED from Heraeus-Clevios was used. It has a PEDOT-to-PSS ratio of 1:6 and a resulting nominal work function of 5.2 eV when dried. [38] Acetone and isopropyl alcohol (IPA) for substrate cleaning were purchased by VWR Chemicals (both have >99% purity). Anhydrous 1,2-dichlorobenzene (1,2-DCB) (purity >99%) was purchased from Sigma-Aldrich and was used as solvent for the organic semiconductors. Teflon-coated magnetic stirrer bars (purchased from Sigma Aldrich) were used to aid dissolution. For the evaporation of the electrodes, silver granules (purity >99.99%, size 1-3 mm) were supplied by Sigma-Aldrich. Tungsten boats from Kurt-Lesker Company were used as evaporation source. Lead frame (used as electrical connection legs to the device) and cover glass slips (for encapsulation) were purchased from Ossila Ltd.. Two-component epoxy-resin (UHU brand) was used for encapsulation. Polished fused quartz substrates (Spectrosil) (11 mm diameter, 1.1 mm thickness) were purchased from Heraeus Quarzglas GmbH. Silicon substrates (20 mm x 20 mm) were cut from (400) silicon wafers purchased from Siegert Wafer.

The polymer/fullerene solutions were prepared at least one week before fabrication of the solar cells to allow complete dissolution of the materials. The substances were weighted under UV-filtered light in ambient air. Any further processing steps were performed under inert gas (argon 5.0) conditions. All solutions were prepared with anhydrous 1,2-DCB as solvent and stirred at 70°C for at least seven days. The blend solutions were prepared in two compositions, namely with F8T2-to-ICBA ratios of 1:1 and 1:4 for each of the F8T2 derivatives P1, P2 and P3, respectively. For the solutions with a weight ratio of of 1:1, a total concentration of 18 mg/ml each was used. For solutions with a weight ratio of of 1:4, concentrations of 10 mg/ml F8T2 and 40 mg/ml ICBA were used.

Solar cells:

The pixelated ITO anode substrates were cleaned in an ultrasonic bath for 10 minutes in acetone and IPA, respectively, and finally dried in a CO_2 stream. To achieve desired low work function of the ITO, the surface was activated by O_2-plasma treatment (10 min., power of 100 W). The plasma etcher is shown in figure 4.1 a. Immediately after plasma-etching the PEDOT:PSS electron blocking layer was deposited from (aqueous) solution (sonicated and filtered by a 0.2 µm PP filter) via spin-coating. A spin-speed of 4000 rpm for 40 seconds was chosen, which lead to an ideal layer thickness of around 73 nm. The used spin coater is shown in figure 4.1 b. Subsequently, the films were left to dry under argon flow at a temperature of 200°C for at least half an hour to remove the water from the layer. The used heating stage is illustrated in figure 4.1 c. It was built in house and consists of a hotplate with a temperature measuring unit, a valve for argon, a quartz glass cylinder and a cap with a pressure measuring unit. To avoid water uptake by the strongly hygroscopic PSS after drying, the dried substrates were immediately transferred to inert environment (glovebox, argon 5.0). All further processing was done under inert gas conditions to avoid degradation of the organic semiconductors by photooxidation. The active layer was deposited on top of the PEDOT:PSS from solution by spin coating. Therefore solutions were applied onto the substrates by microliter pipette (as illustrated in figure 4.1 d), with 100µl each. The spin speeds and durations for every D/A combination varied in order to obtain an optimum thickness of around 100 nm. The parameters are listed in table 4.1.

Table 4.1: *Spin speeds and times for the used material combinations*

Materials	Spin speed	Time
P1 : ICBA (1:1)	30 rps	90 sec
P2 : ICBA (1:1)	27 rps	90 sec
P3 : ICBA (1:1)	27 rps	120 sec
P1 : ICBA (1:4)	25 rps	90 sec
P2 : ICBA (1:4)	25 rps	90 sec
P3 : ICBA (1:4)	24 rps	120 sec

To study effects of annealing on the polymer blend, one part of the samples was left pristine, while the other was annealed on a hotplate at 70° for 10 minutes, as shown in figure 4.1 e. The final layer of the solar cells was the silver cathode, deposited by thermal evaporation. Since for the Ossila-System [38] pixelated anode substrates are used, only one wide cathode stripe is required. Note: the Ossila system requires that the wide ITO contact-stripe on the substrate (used to connect the device legs to the cathode) is cleared from eventual depositions as shown in figure 4.1 f. For evaporation, the samples were placed in a shadow mask (figure 4.1 g) and installed in the evaporation chamber. The thermal evaporator (shown in figure 4.1 h) is custom-built and fitted into a glovebox. It consists of an aluminum bottom plate holding the vacuum/venting flange and electrical connections for the resistive heating of the evaporation source. The aluminum top plate holds the mask holder (for the samples), the manual shutter and the quartz oscillator. The actual chamber is a quartz glass cylinder of diameter 160 mm and height 250 mm. As evaporation source, regular tungsten boats were filled with silver granules. The evaporation chamber was evacuated by rotary vane and turbo molecular pump to the high vacuum range (exact values can be found in the table 4.2).

Table 4.2: *Evaporation rates and pressures when the evaporation was started*

Materials	Pressure	Evaporation rate
P1 : ICBA (1:1)	$3.2*10^{-5}$ mbar	11.1 nm/min
P2 : ICBA (1:1)	$1.2*10^{-5}$ mbar	6.3 nm/min
P3 : ICBA (1:1)	$2.9*10^{-5}$ mbar	9.1 nm/min
P1 : ICBA (1:4)	$3.4*10^{-5}$ mbar	8.3 nm/min
P2 : ICBA (1:4)	$1.6*10^{-5}$ mbar	4.8 nm/min
P3 : ICBA (1:4)	$1.3*10^{-5}$ mbar	12.5 nm/min

The silver was evaporated with rates between 6.3 and 12.5 nm/min (exact evaporation rates can be found in table 4.2), to a final thickness of around 100 nm. The thickness was monitored by a quartz monitor. To facilitate the electrical measurement of the devices, lead frame (legs) were connected to the substrate by using a customized screw clamp (figure 4.1 i). Finally, the solar cells were encapsulated with 2-component epoxy resin and a cover glass slip (figure 4.1 j) to protect from degradation while performing measurements in air.

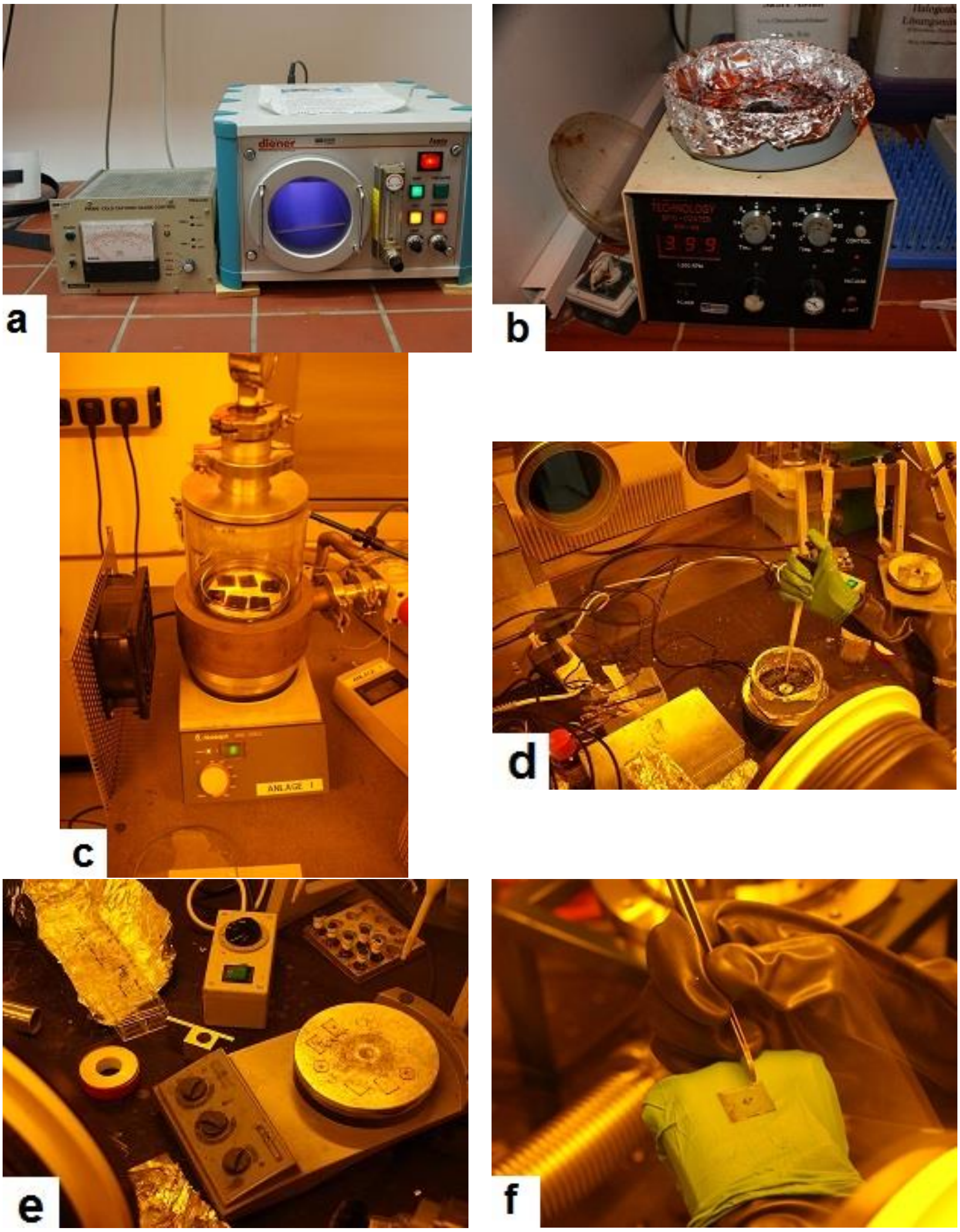
a
b
c
d
e
f

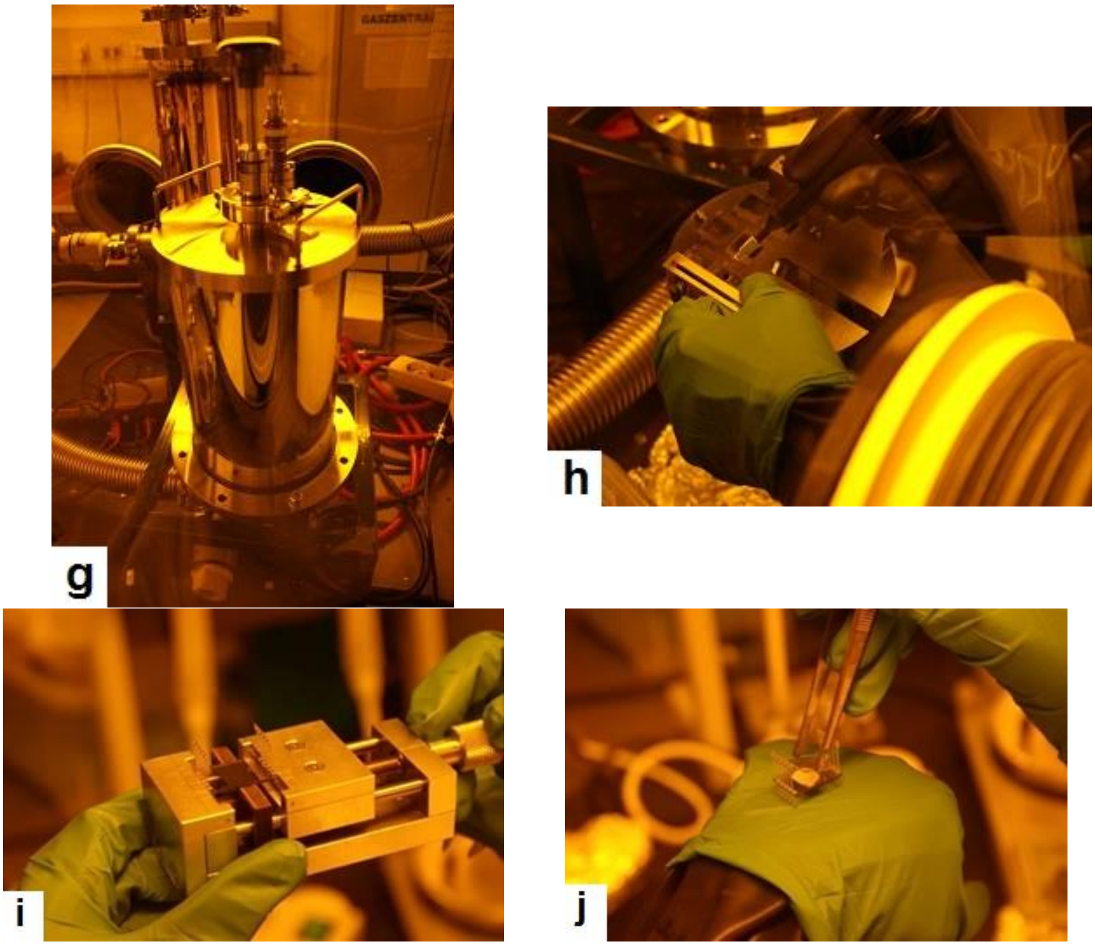

__Figure 4.1:__ Apperatures and processes used for the fabrication of solar cells: plasma etcher (a), spin coater (b), heating stage (c), applying of the active layer (d), hot plate (e), cleaning the cathode ITO contact-stripe (f), evaporation chamber (g), shadow mask (h), screw clamp (i) and encapsulation with resin and a cover glass slip (j)

Fused quartz substrates

Fused quartz substrates (spectrosil) were used for UV-VIS experiments, because of their excellent transmittance not only in the visible, but also in the ultraviolet wavelength range. Also AFM imaging and profilometer thickness measurements were performed on films on spectrosil. Also these substrates were cleaned in acetone and IPA with the same procedure as for the solar cell substrates. They were coated with active layers of the same composition of solutions mentioned above and spin-coating with the same parameters (table 4.1), but by applying only 65µl per substrate.

Samples for XRD:

For XRD measurements, silicon substrates were cleaned in IPA in the ultrasonic bath for 10 minutes and dried in a CO_2 stream. Afterwards they were exposed to O_2-

plasma under the same conditions as the substrates for solar cells. Active layers of the same composition as for the solar cells were deposited in argon atmosphere. Here the films were applied via drop casting, because XRD required higher film thickness.

Samples for PL and TCSPC:

Solutions with polymer-only (16 mg/ml) and polymer:ICBA with a 1:1 ratio (16 + 16 mg/ml) were prepared one day before film fabrication. They were stirred at 70°C overnight. Anhydrous 1,2-DCB was used as solvent. Spectrosils were cleaned in IPA in an ultrasonic bath for 10 minutes and dried in a N_2 stream. For each sample, 65µl of the according solution were spin-coated for 60 seconds with 25 rps in nitrogen atmosphere.

4.2 Electrical characterization set-ups

General set-ups:

The sample holder, where each pixel can be selected separately, is shown in figure 4.2. As can be seen in this illustration, the first black switch on each hand side is turned to ground. This means that the electrodes are on ground. This condition was needed for all investigations. For recording current voltage curves a KEITHLEY 2636A was used. All measurements were performed in a black box to protect the sensitive diodes from stray light to not falsify the results.

Figure 4.2: *Sample holder from Ossila*

Dark current:

The dark current measurements were the first investigations that were performed after fabrication of the solar cells to observe their diode behaviour in their virgin and undegraded state. For dark current measurements, the sample holder was placed in a black box and additionally covered with a black cloth. Current-voltage curves were recorded in a voltage range from -1 to 1.8 V with a step size of 0.02 V.

External quantum efficiency:

An illustration of the quantum efficiency setup can be seen in figure 4.3. Monochromatic light is generated with a 250 Watt tungsten halogen broad band white light source that was built in house (fig 4.3, no. 7). It has a wavelength resolution of 5 nm. The monochromatic light beam then passes a filter wheel (Fig 4.3, no.6) with 3 relevant filter positions, blocking the beam for dark current measurements, passing for wavelengths smaller than 650 nm and filtering with a red long-pass filter for wavelength larger than 650 nm (to block higher orders from the monochromator). The beam is diverted by beam splitter (Fig. 4.3, no.4). It splits the beam intensity in a ratio of 30% to 70% and leads these two fractions to two separate photodiodes, focussed by lenses (no.3). One diode (no. 1) is a calibrated diode (wavelength dependent light sensitivity known), another is used as the reference diode (no. 2). Before performing quantum efficiency measurements, the assembly is calibrated regarding light intensity per wavelength on both two beam paths (and saved in the computer). During the measurement, the solar cell is placed in one beam path instead of the calibrated diode. This way, the intensity of an incoming light beam on the reference diode can be used to reference back to the intensity of the light spot illuminating the solar cell, allowing calculations for electrons extracted per incoming photon. For technical reasons, a mirror (no.5) was used during the measurements for directing the focussed light spot onto the sample holder and onto the particular solar cell pixel measured. For each pixel first the external quantum efficiency measurement was done, which records the short circuit current over wavelength.

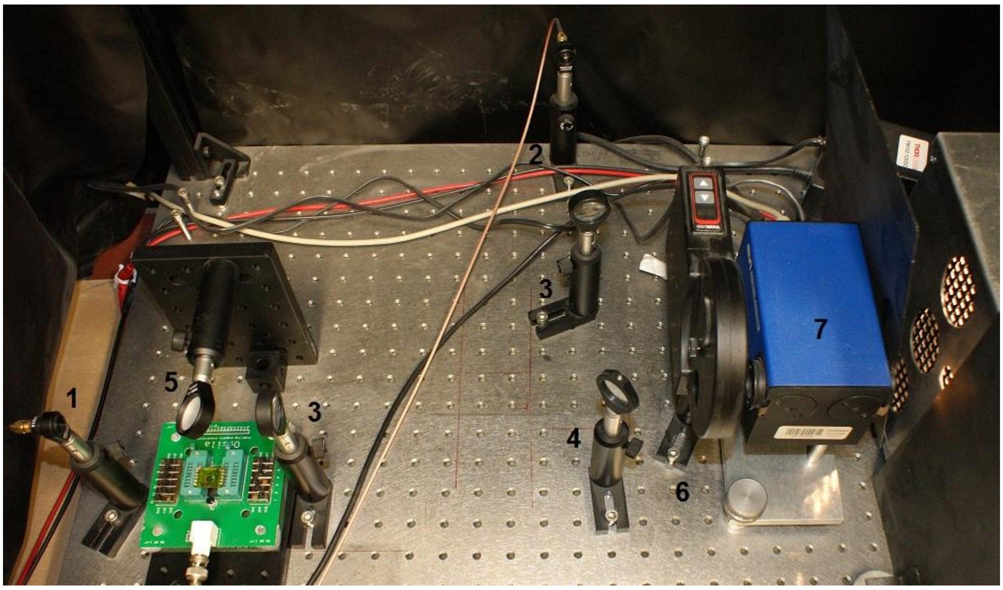

Figure 4.3: *Set-up for EQE measurements*

Photocurrent under simulated solar conditions:

Solar simulations were performed under AM 1.5G conditions. The used solar simulator is by ABET Technologies, model number 10500. An illustration can be seen in figure 4.4. The system produces a collimated 25 mm beam. [39] Its rating is ABB, which means a spectral match in each interval between 0.75 and 1.25, an irradiance spatial non-uniformity of 5% and a temporal instability of 5%. To perform the measurements the sample holder with the solar cell was placed under the light spot. Each of the solar curves was recorded in 0.02 Volt steps for good resolution. The investigated range was between -1 Volt and 1.8 Volt.

Figure 4.4: *Solar simulator by ABET Technologies*

4.3 Photophysical characterization set-ups

Optical absorption:

The absorption spectra were recorded with the UV-VIS UV1800 spectrophotometer by Shimadzu. It is illustrated in figure 4.5. On the left hand side an illustration of the sample holder is shown and on the right hand side an illustration of the whole machine. For the measurements, two Spectrosil substrates, one with an active layer (sample) and an empty (reference), were fixed to the sample holder. Note: sample holder for cuvettes was adapted in the way that substrates per taped to the cuvette holder window with layer to the front (beampath: source→film→spectrosil→cuvette holder→detector). Due to the dual-beam characteristic of the spectrophotometer the reference was constantly measured together with the sample, allowing low risk of inaccuracies due to fluctuations. The reference spectrum was internally substracted. The measurements were performed in absorption mode in a wavelength range from 190 to 1100nm.

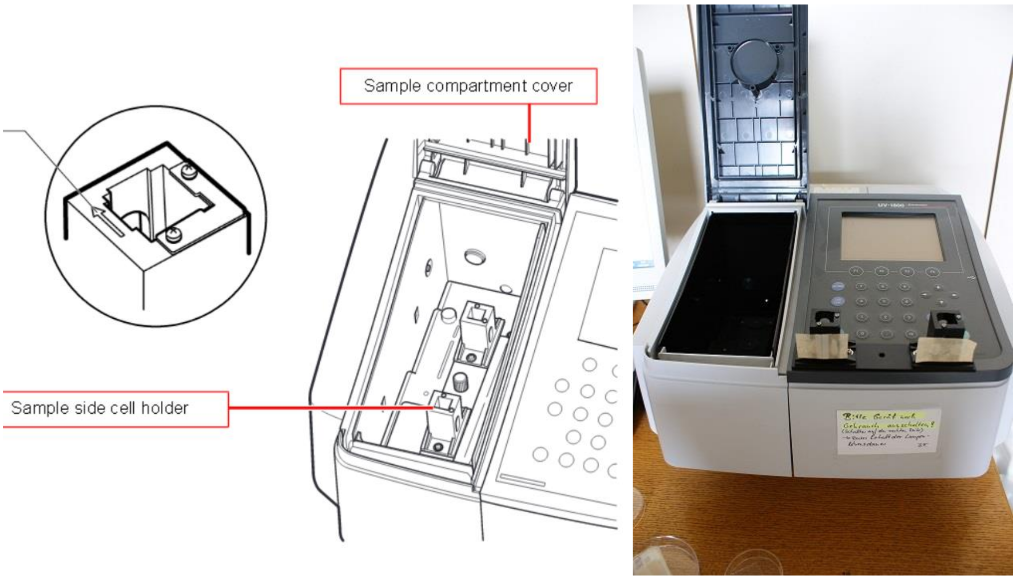

Figure 4.5: *Schematic illustration of the sample holder (left) and UV-VIS spectrometer by Shimadzu (right)*

Photoluminescence and time correlates single photon counting:

Photoluminescence (PL) spectra and lifetimes of the organic layers were studied. Lifetimes were determined from the emission decay characteristics derived from time correlated single photon counting (TCSPC). The PL/TCSPC system consisted of a vacuum-cryostat with optical access as the sample chamber (shown in figure

4.6). Attached to the top of the cubic chamber is a vacuum hose, connected to a vacuum pump (shown on the left hand side). During measurements, the chamber was under vacuum of $4 * 10^{-4}$ mbar, to avoid photooxidation reactions of the thin film with air. The optical access windows of the chamber were in 90° to each other on two sides of the cube. Thereby one window was used for the incoming laser beam, the other for collecting the emitted light. The sample in the vacuum chamber was positioned in an angle of 45° to the incoming beam. For recording PL spectra, the samples were irradiated by a laser beam with a wavelength of 407nm for 1 sec and the emitted light passed through a filter (to cut off the excitation wavelength) and a system of lenses onto a spectrometer/detector. On the right hand side of figure 4.6 the beam path with a system of mirrors and lenses to direct and focus the emitted light from the sample to the spectrometer/detector or other analytic units, can be seen. To record the TCSPC characteristics, the samples were irradiated by a pulsed laser diode with (same wavelength) with pulses of 100 ps full-width at half-maximum. The decay rates were probed at desired wavelength. A picosecond pulsed diode-laser source with a laser diode pulse driver model PDL 800-B from PicoQuant were used. As detection unit the SpectraPro-2500i from Acton Research Corporation was used.

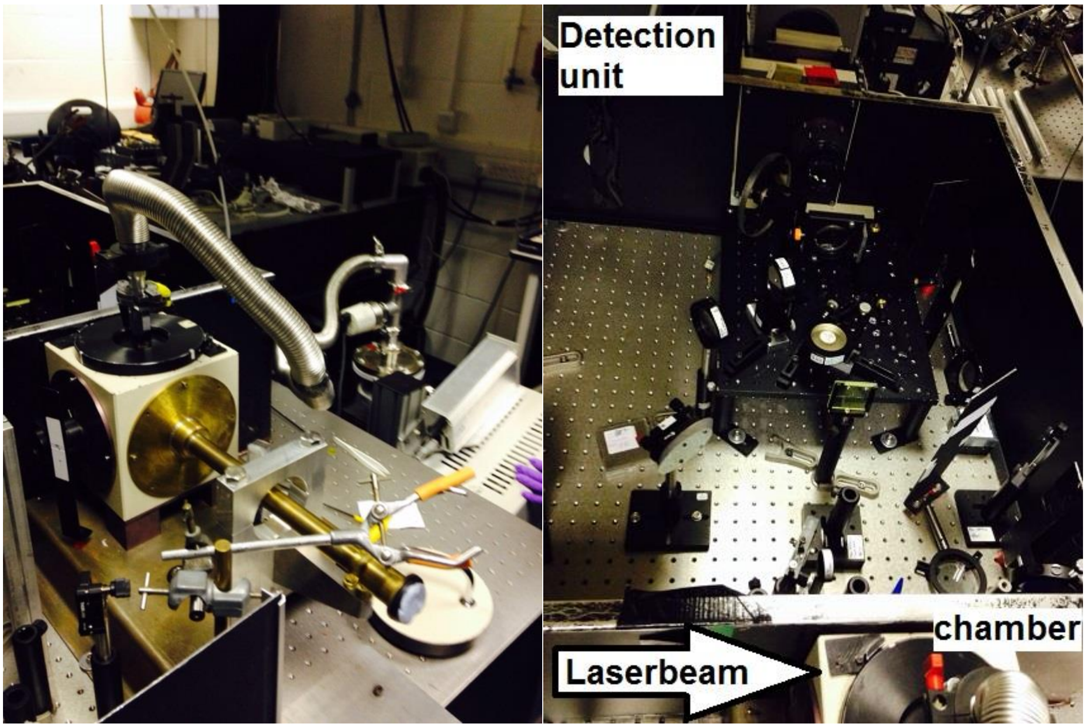

Figure 4.6: *TCSPC set-up: detection chamber (left) and lens system (right)*

Electroluminescence:

For detecting the electroluminescence emission the sample was placed in a black box, to protect the measuring unit from any stray light. The set-up consists of the source measure unit KEITHLEY 236, an sample holder from Ossila (see figure 4.2), an Oriel photo detector with a monochromator and a PC with the programme “andorMCD”. For calibration of the set-up an Ar-Hg vapour discharge lamp was used.

4.4 Morphological characterization set-ups

Profilometry:

A technique to determine the thickness of the active layer is mechanical profilometry. The used stylus profilometer was a Dektak ⅡA, which is shown in figure 4.7. It can be used to record line profiles of the surface topography of a sample. Given a step or trench between film surface and substrate (e.g. by making a scratch) film heights between 10 nm and 100 µm can be measured. [40] For thickness measurements on thin films the active layer was deposited on a spectrosil substrate and scratched with the tip of metal tweezers to create a measurable gap. The apparature consists of a scanning unit (figure 4.7 no. 1) and a display/computer unit (figure 4.7 no. 2). The scanning unit moves a metal stylus with diamond tip mechanically over a selected area of the substrate, where the scratch is. The monitor shows the profile of the line scan. Film height can be analysed by placing two cursors and get a differential reading of the height difference. Accuracy of this method is about ±10 nm, depending on the film’s hardness.

Figure 4.7: *Illustration of the Dektak ⅡA*

Atomic Force Microscopy:

Morphology and phase separation of the donor/acceptor blends were investigated with an atomic force microscope (AFM). The used AFM is the Nanosurf Easyscan 2, shown in figure 4.8. Number 1 shows the scan head, which was a 7µm type scan head. Number 2 labels the sample holder that was connected magnetically to the metal plate below to protect the cantilever. The damping table, where the AFM was placed on to protect it from any vibrations, is marked by number 3. All scans were taken in tapping mode. 256 points per line were scanned and each line was scanned for 2 minutes.

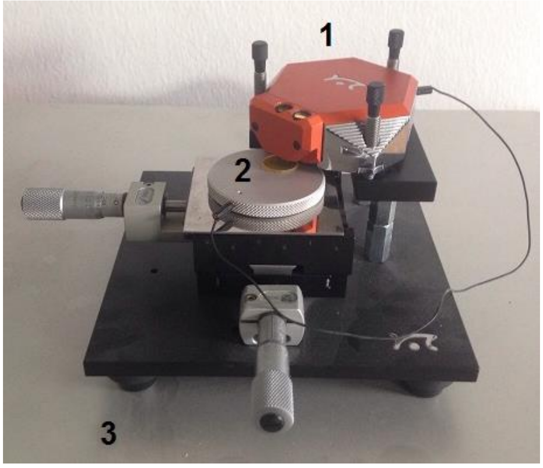

Figure 4.8: *Illustration of the AFM is the Nanosurf Easyscan 2*

Light Microscopy:

Optical microscopy was used to investigate the homogeneity of the organic films. Also undissolved material cluster, agglomerations and delaminations can be detected. The used microscope is the BX52 from Olympus and shown in figure 4.9. The used set up consists of a camera, model C-5060 Wide Zoom from Olympus (no. 1). The ocular (no. 2) provides a magnification of 10x. Number 3 shows a revolver with four different objectives, with magnification of 5, 20, 50, and 100x. The specimen stage is labelled by number 4 and the two light sources for transmission and reflecting mode are labelled by number 5. Number 6 shows a PC where the software Olympus DP-Soft 5.0 was used to edit the taken pictures.

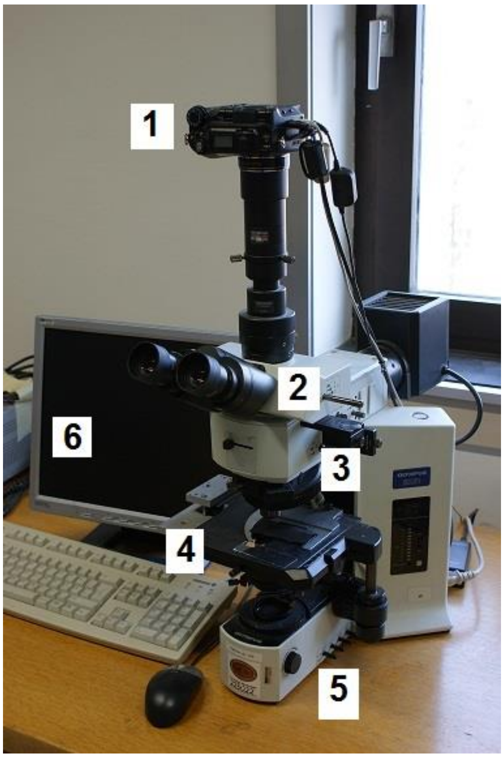

Figure 4.9: *Illustration of the microscope BX52 from Olympus*

<u>Grazing-Incidence X-Ray Diffraction:</u>

The X-ray diffraction measurements were performed at the synchrotron facility BESSY II with beamline KMC-2. A wavelength of 1 Å was used and the exposure time was 900s for each sample. A schematic illustration of the setup is shown in figure 4.10. As area detector the Bruker Vantec 2000 MikroGap was used, labelled by no. 1. Number 2 shows the chamber where the samples were located. The 6-axis HUBER goniometer is labelled with no. 3 and the beamline by no.4. To convert the detected scattering data into the reciprocal space, a tool named “xrayutilities” [41] was used.

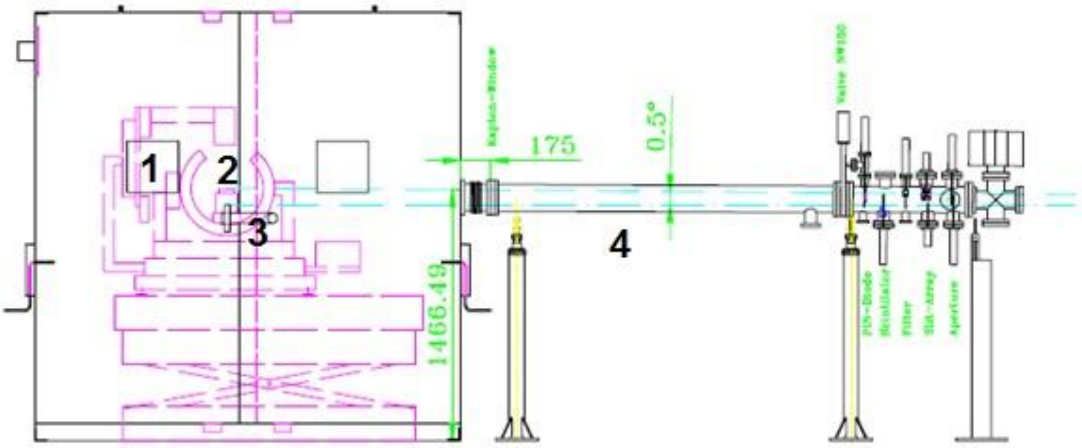

Figure 4.10: *Schematic set-up for the X-ray measurements*

5 Results and Discussion

5.1 Dark current

To get information solely about the diode behaviour of the solar cells, the current-voltage-characteristics without illumination were recorded. The according data were plotted in semi-logarithmic scale to facilitate analysis. Figure 5.1 shows the results for D/A 1:1 blends. The off-zero voltage shift for both P1 curves is a measurement artefact (originating from the SMU). For all three blends, clear symmetric ohmic behaviour can be seen between -0.25 and +0.25 V. In reverse bias (V < 0 V), P2 and P3 blends show for the current density at 0.5 V values of 10^{-4} and $2*10^{-4}$ mA/cm^2, respectively. These values are significantly higher than for P1 blends, which show at 0.5 V current densities of $2*10^{-6}$ mA/cm^2 for the annealed and the not annealed blend. This could indicate presence of higher density of leakage pathways in these devices. In forward bias, P2 and P3 show some kind of dip in the shape of the IV curve at 0.8 and at 1.0 V, respectively.

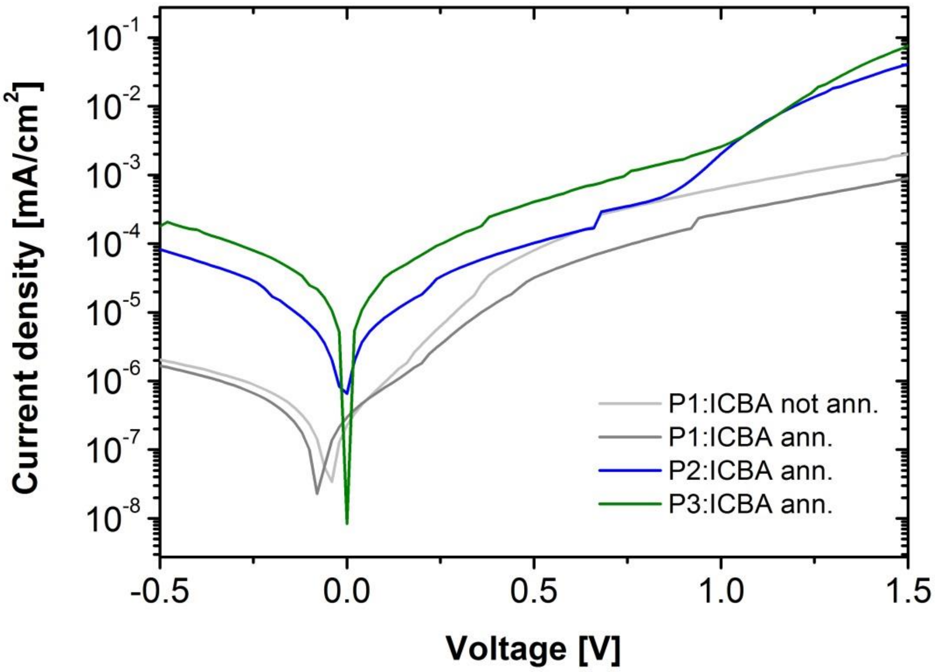

Figure 5.1: *Semi-logarithmic dark current curves, derived from blends with a D/A ratio of 1:1*

That indicates charge trapping behaviour. In these traps charge carriers got stuck and get released for an energy that is larger than the energy of the trap. In the space-charge limited current region of the cell (above 1.3 V), the slopes of the current of P2 and P3 are higher than for P1 (P1<P2<P3), which indicates a better majority charge carrier mobility in the device. In the case of P1, the IV characteristics of pristine and annealed films show no significant difference in the slope and therefore the mobility, different to the expectations for mobility enhancement by thermally induced molecular reorganization.

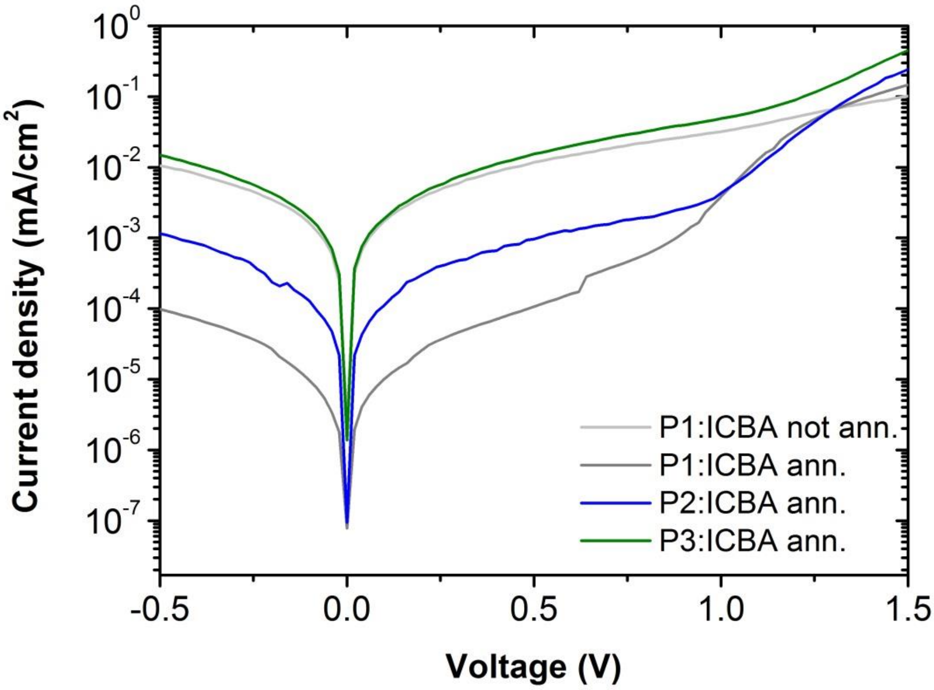

Figure 5.2: *Semi-logarithmic dark current curves, derived from blends with a D/A ratio of 1:4*

The dark current curves derived from cells with a D/A ratio of 1:4 can be seen in figure 5.2. Very high dark current is obtained for the not annealed P1 blend and the P3 blend, with values of about 10^{-2} mA/cm^2 for both of them at 0.5 V. Followed by P2 with 10^{-3} mA/cm^2 and the annealed P1 with 10^{-4} mA/cm^2, which is more beneficial for device performance. Like for the P2 and P3 blend with a D/A ratio of 1:1, also here both devices show a trap-induced dip in the IV characteristic, but shifted to higher voltages (P2~0.9 V, P3~1.1 V). Further, the annealed P1 device for this blend composition also shows an according dip at 1.0 V.

5.2 External quantum efficiency

The maximum external quantum efficiencies (*EQE*) of the various F8T2:ICBA blend devices can be found in table 5.1. It contains the values for the 1:1 and 1:4 blend compositions for the three different F8T2s for annealed systems and also (for comparison) for a not annealed 1:1 P1 blend. The values are reproducible and representative for each material combination. The *EQE* values between 0.07% and 0.50% *EQE*, are generally far below the ones reported in literature of over 30% for similar systems like F8T2:ICBA [42]. Reasons for that could be phase separation issues, energy level mismatch, transport issues or impurities in the materials. In figure 5.3 and 5.4, the dark current-corrected and normalized *EQE* spectra of the blends for weight ratios of D:A=1:1 (figure 5.3) and 1:4 (figure 5.4) are shown. The normalization was done to facilitate the visibility of peak shifts. According peak shifts allow conclusions about the relative conjugation lengths of the of the polymers within the blends and thus indicate the degree of long range order (crystallinity) in the films.

Table 5.1: *Material combinations and according EQE values*

Materials	**Annealed**	**EQE (%)**
P1:ICBA (1:1)	No	0.20
P1:ICBA (1:1)	Yes	0.22
P2:ICBA (1:1)	Yes	0.13
P3:ICBA (1:1)	Yes	0.30
P1:ICBA (1:4)	No	0.28
P1:ICBA (1:4)	Yes	0.43
P2:ICBA (1:4)	Yes	0.07
P3:ICBA (1:4)	Yes	0.50

Figure 5.3 shows that the *EQE* of the not annealed P1:ICBA cell has a maximum at 480 nm. With annealing, the maximum is clearly shifted to a wavelength of about 510 nm. This red shift indicates a longer conjugation length of the polymer within this blend and therefore a higher degree of order. In comparison, the device made of P2:ICBA shows a strong shift to smaller wavelength of about 60 nm compared to the pristine P1:ICBA. Also P3:ICBA shows a shift of around 40 nm in the same direction. This is evidence of P2 having the shortest conjugation length in the blends of all materials. This behaviour is obviously a result of the molecular geometry of the

material, as the branched side-chains are expected to promote disorder in the film and due to that fact, the P2-blend seems to be the most amorphous one. The conjugation length and thus the degree of order in the film fabricated from P3 is intermediate between P1 and P2. That reflects well the fact that P3 is a mixture of P1 and P2 building blocks, having both, straight and branched side chains. Looking at the values of the *EQE* for the blends with a weight ratio of 1:1, the highest performance is obtained for P3. This appears reasonable, due to the fact that P1 is known for strong crystallisation (producing too large phases and massive grain boundaries for efficient operation) and P2 being "too amorphous" for good charge carrier transport.

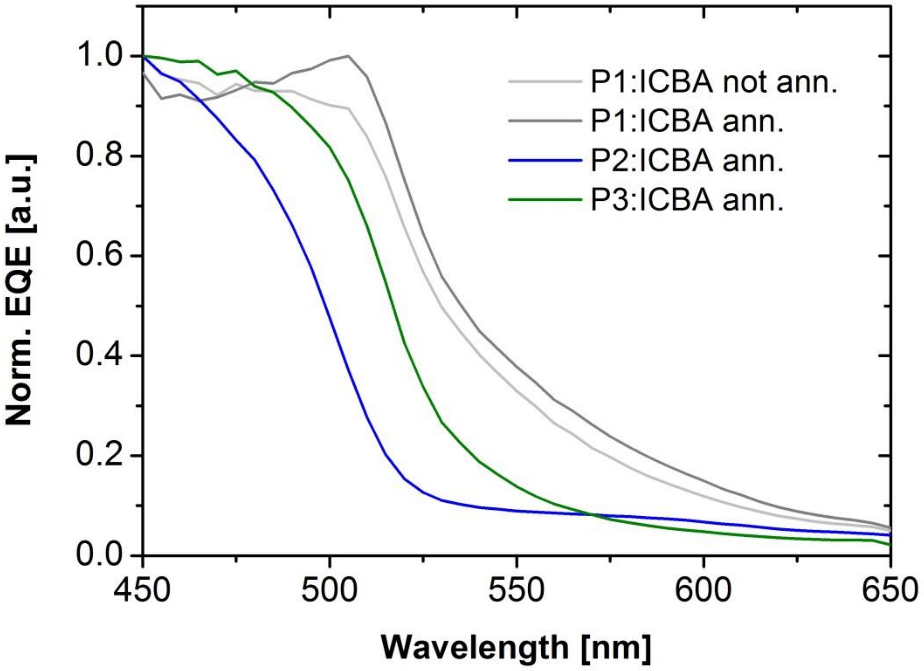

Figure 5.3: *Normalized EQE for blends with a D/A weight ratio of 1:1*

Devices with annealed and pristine 1:4 blends of P1:ICBA have their maximum in the *EQE* spectrum at a wavelength of about 475 nm (figure 5.4). Thereby no significant difference in shape and no shift in wavelength as in blends with a weight ratio of 1:1 is observed. The *EQE* maxima of according P2 and P3 blend devices are slightly below 475 nm. So, both of them are blue shifted, which is better visible at the flank of the *EQE* peak. Compared to the 1:1 blends in figure 5.3, the shifts are far less strong with values of around 5 nm. But also in this case P2 shows the strongest blue shift and therefore the shortest conjugation length and the highest grade of disorder. Again, this is followed by P3, with an intermediate conjugation length and order in the film between the other two polymers. The values for the *EQE*s show that annealing clearly improves the performance for P1. The poorest performance is obtained for P2 blends and the highest ones for P3 blends, as it was seen for blends with a D/A weight ratio of 1:1, before.

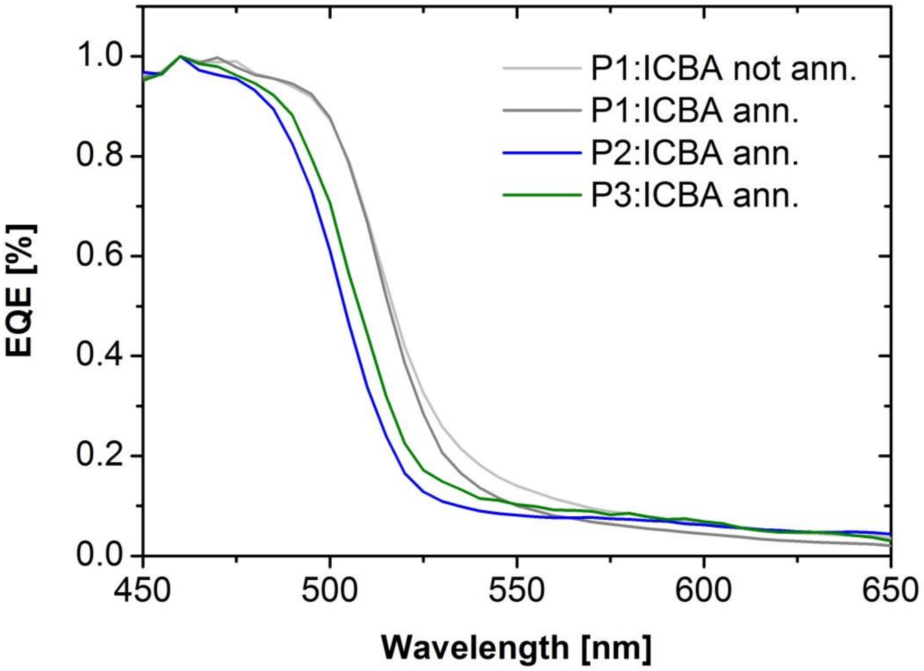

Figure 5.4: *Normalized EQE for blends with a D/A weight ratio of 1:4*

5.3 Photocurrent

For illustrating the photocurrent curves under AM 1.5G conditions, the recorded light currents were dark current-corrected. The graphs recorded for the different F8T2:ICBA blends with weight ratio of 1:1 are shown in figure 5.5. The according fill factors (*FF*) and efficiencies η are summarized in table 5.2.

Table 5.2: *Material combinations and according fill factors and efficiencies*

Materials	Annealed	FF (%)	η (%)
P1:ICBA (1:1)	No	26	0.02
P1:ICBA (1:1)	Yes	29	0.03
P2:ICBA (1:1)	Yes	33	0.07
P3:ICBA (1:1)	Yes	31	0.07
P1:ICBA (1:4)	No	30	0.04
P1:ICBA (1:4)	Yes	35	0.09
P2:ICBA (1:4)	Yes	29	0.04
P3:ICBA (1:4)	Yes	28	0.05

The pristine P1 sample shows in its characteristic the lowest short circuit current density (J_{SC}) of -0.10 mA/cm^2, the weakest increase in forward bias and an open circuit voltage of 0.79 V. The annealed P1 blend shows the same shallow increase in forward bias, but in comparison a higher J_{SC} of -0.12 mA/cm^2 and a slightly smaller V_{OC} of 0.77 V. Here also subtle “S-shape” behaviour near the open-circuit point is visible. This “S-shape” is typically an indication for charge blocking at the contacts or interfaces or also for unbalanced charge mobilities (electrons vs. holes). The annealed P2 blend shows clear improvement of the parameters compared to both P1 blends. It has a V_{OC} of 0.89 V and a J_{SC} of -0.23 mA/cm^2. Compared to the P2 blend, the P3 blend shows an even higher J_{SC} of -0.25 mA/cm^2, but a smaller V_{OC} of 0.86 V. Both, P2 and P3 show decent rectangularity of the curve and a steep rise in current under forward bias, reflecting the suggested higher charge mobility in these blends seen from the space-charge limited current region in dark current.

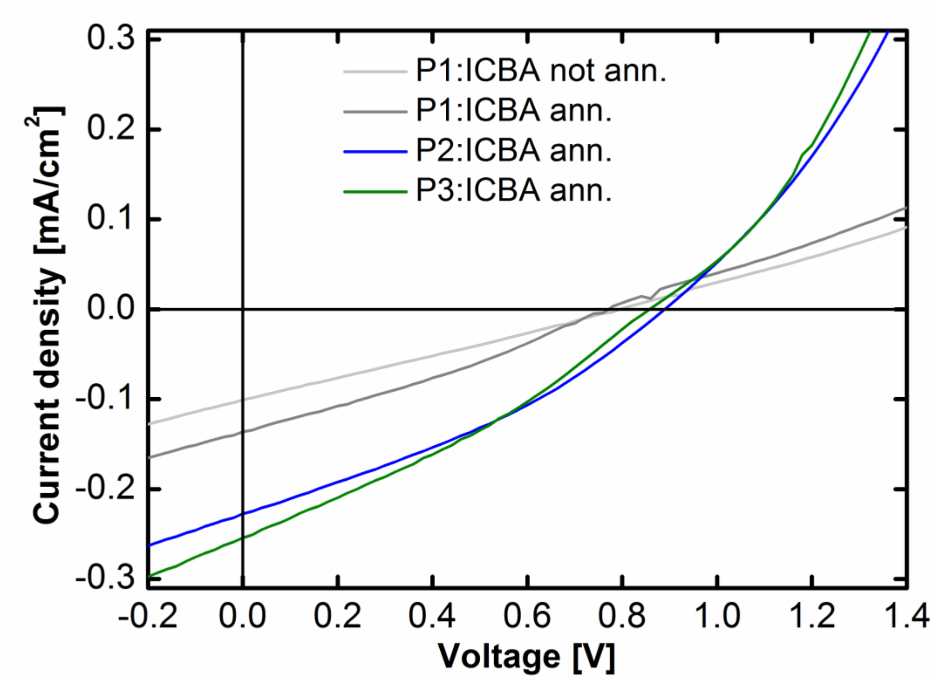

Figure 5.5: *Dark current corrected light IV-curves (AM 1.5G conditions) derived from blends with a weight ratio of 1:1*

The IV-curves derived from blends with a donor acceptor ratio of 1:4 show different behaviour as for 1:1, as illustrated in figure 5.6. Both P1 blends, pristine and annealed, show an improvement in photocurrent compared to the 1:1 blends. The not annealed blend has a current density of -0.14 mA/cm^2 and the annealed one of -0.26 mA/cm^2. Also the open circuit voltage shows larger values of around 1 V for both of the blends. P2 and P3 have both considerably lower J_{SC} with values of -0.16 and -0.22 mA/cm^2, respectively. The open circuit voltages are smaller than for the P1 blends -0.88 V for P2 and 0.79 V for P3. As for curves derived from blends with a weight ratio of 1:1, also here both P1 blends show a “S-shape” behaviour around the open-circuit point.

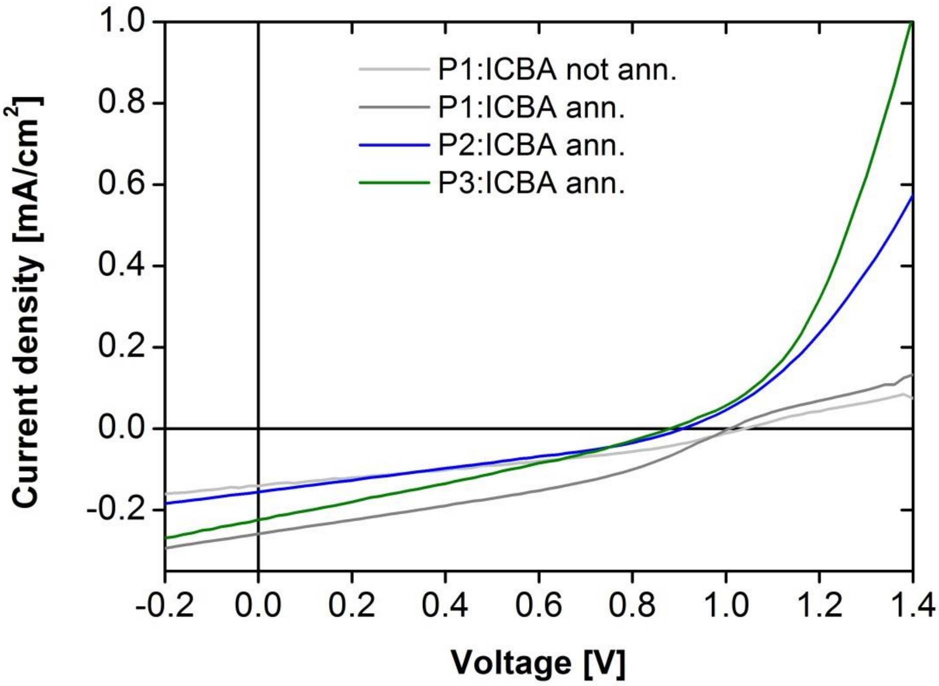

Figure 5.6: *Dark current corrected light IV-curves (AM 1.5G conditions) derived from blends with a weight ratio of 1:4*

5.4 Electroluminescence emission behaviour

In figure 5.7 and 5.8 the normalized electroluminescence (EL) emission is shown for blends with a D/A weight ratio of 1:1 and 1:4, respectively. For all F8T2s and blend compositions, EL was detected from cells biased in forward direction.

For curves derived from blends with D:A of 1:1, the shape of the emission is more or less similar between the different samples with slight differences in intensity of the different peaks and small changes in position. There is a rather sharp main peak at around 750 nm, with a full-width-at-half-maximum (FWHM) of about 50 nm, which can be assigned to the emission of the F8T2. A second smaller but broader peak with FWHM of about 90 nm is located at around 850 nm and is originating from the ICBA [42]. Considering that the emission spectrum must be the envelope of several Gaussian-shaped emissions, it is obvious that a third, much broader emission must be superposing the red tail of the electroluminescence emission spectrum. It is suggested that this originates from the emission of the CT state, which is expected to peak between 850 and 1150 nm (calculated from cross-band gap is 1050 nm) and thus was not in the detectable range.

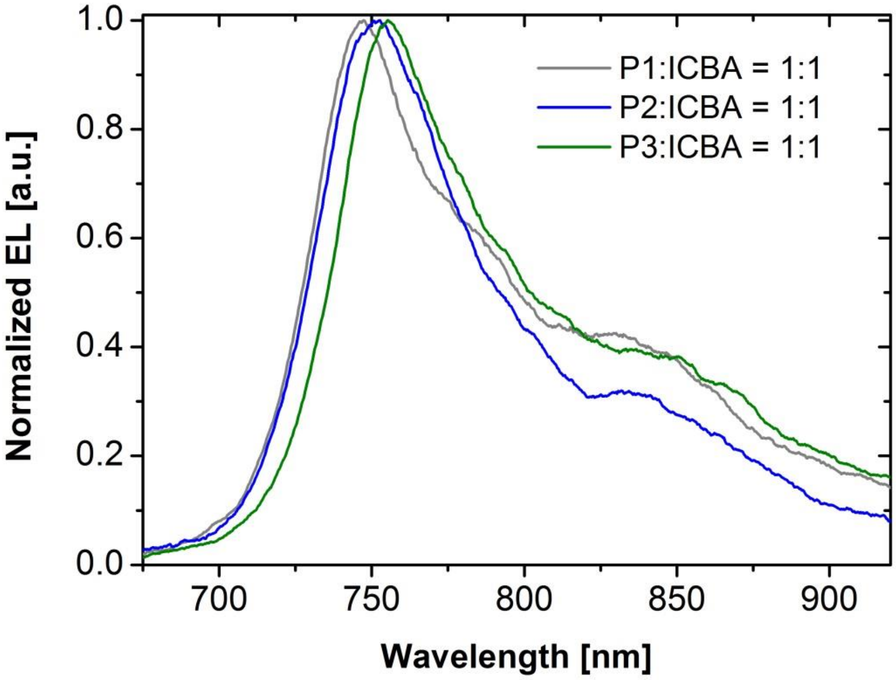

Figure 5.7: *Normalized EL emission for blends with D:A ratio of 1:1*

Figure 5.7 shows the highest peak to be at 750 nm for P1, at 755 nm for P2 and at 760 nm for P3. Shifts to the blue wavelength region here indicate a higher grade of crystallinity in the film. Therefore P1 seems to exhibit the highest grade of order and P3 the least. This is unexpected with respect to the other results. It might also be possible that the shift is a result of the energy levels the F8T2s (note: though the largest contribution comes from the conjugated backbone and its building blocks, also side chains can induce changes in the band gap due to electron-withdrawing or donating nature). Or it might be an effect of the underlying CT emission. It seems not to be a measurement artefact, as the emission is reproducible. The emission around 840 nm from ICBA has the lowest intensity for P2, while P1 and P3 are slightly higher but equal. Due to the high intensities in the ICBA tail, the appearance of a charge transfer-state (CT-state) is suggested for P1 and P3.

Figure 5.8 shows the polymer emission peak at 755 nm for P1, at 760 nm for P3 and at 765 nm for P2, derived from blends with D/A ratio of 1:4. In contrast to the 1:1 blends, P2 indicates the least order in the film. At 850 nm, emissions from ICBA appear, with the highest intensity for P1 blends. Also in these blends a CT-state emission might form the background for wavelength larger than 800 nm.

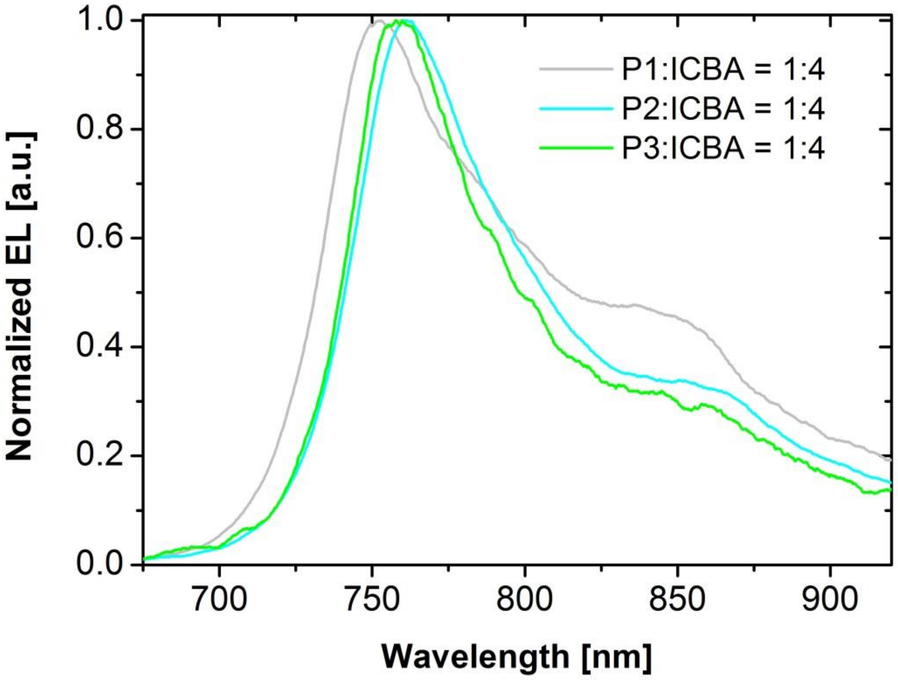

Figure 5.8: *Normalized EL emission for blends with D:A ratio of 1:4*

5.5 Emission behaviour and decay characteristics

In figure 5.9 the normalized PL intensity over wavelength is illustrated for the three pure F8T2 polymers. Four vibronic peaks are visible, located at 500 nm (*0-0*), 550 nm (*0-1*), 580 nm (*0-2*) and 640 nm (*0-3*), respectively (note: the numbers in brackets indicate the vibrational states of the transition). The spectra were normalized to make the positions of the different peaks better comparable. The measurements of the P1 film show that the first vibronic peak is hardly visible, where the *0-1* and *0-2* peak are quite distinct. This indicates a high degree of crystallinity in the film. Due to the broadening of the emission (measured at room temperature) the *0-3* peak appears in the shape of a shoulder. F8T2-P2 shows the *0-0*, *0-1* and *0-2* peak very pronounced. The *0-3* peak again appears as a shoulder. The *0-0* versus *0-1* peak ratio is increased compared to F8T2-P1. This indicates a higher disorder in the P2 film. The P3 film shows the *0-1* peak as being the most pronounced one. The *0-0* to *0-1* peak ratio is lowered compared to that one of P2, which is an evidence for a lower grade of disorder than for P2, but still a higher one than for P1. This fact reflects P3 being a mixture of building blocks of P1 and P2.

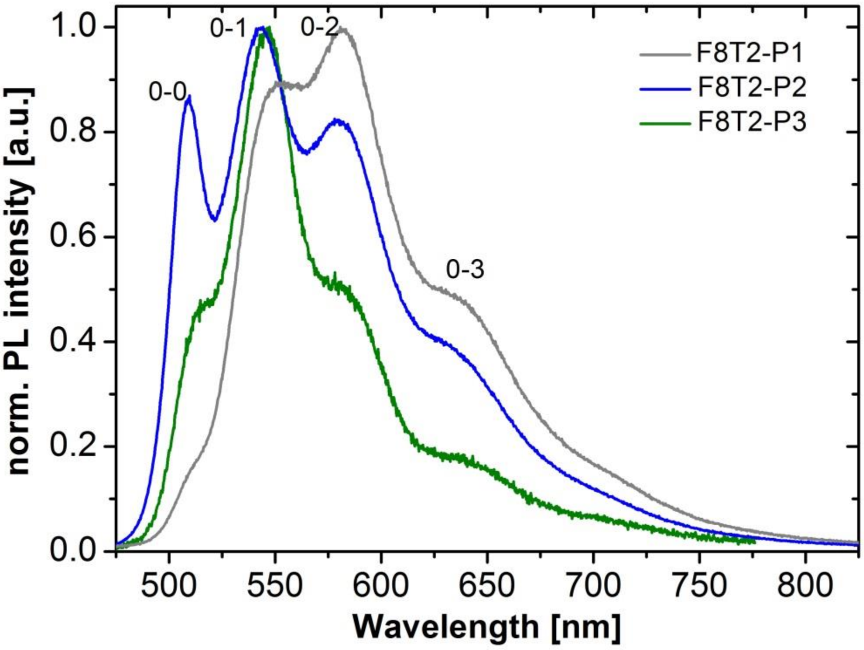

Figure 5.9: *Normalized PL emission derived from polymer-only films*

For investigation of the excited state lifetimes, decay rates were probed at the wavelength of the *0-1*, *0-2* and *0-3* peak shown in the PL spectra for F8T2-only films. The detected TCSPC kinetics are showing a fast and a slow component, thus they had to be fitted bi-exponentially. The original decay curves are shown in figure 5.10 with a logarithmic scale on the y-axis for the counts over the time. The obtained lifetimes are shown in figure 5.13. The derived long-lifetime component varies in the range of 1.00 to 2.25 ns, while the short lifetime components are between 0.25 and 0.38 ns. For a detection wavelength of 550 nm, which corresponds to the *0-1* peak, the values for long and short lived components are quite similar for all three polymers. Only P2 shows a slightly slower decay. At 580 nm and 640 nm the short lived components are all in a very narrow time range, where the long-lived components differ more from each other with increasing wavelength for P2 and P3. This indicates a different grade of order for P1, P2 and P3 blends. P2 decays becoming significantly slower with increasing detection wavelength. This might happen due to triplet formation, as these transitions are slower.

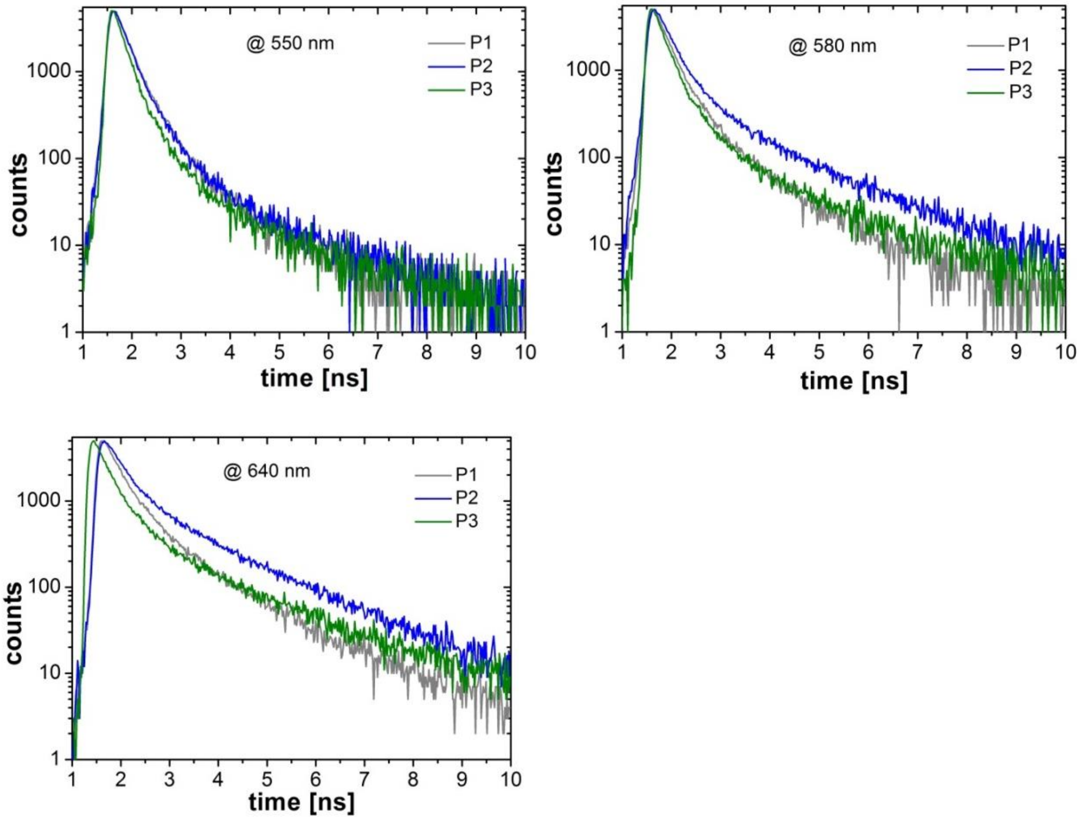

Figure 5.10: *TCSPS lifetime decay curves of polymer only films, detected at 550 nm (top, left), 580 nm (top, right) and 640 nm (bottom, left)*

In figure 5.11, PL spectra of F8T2:ICBA blends (ratio 1:1) are shown. The recorded photoluminescence emission for P1 is illustrated with a magnification of 3 and the one for P3 with a magnification of 4. Normalization was not done, because P1 and P3 would have shown too much noise. Compared to the polymer-only films clear quenching is visible for P1 and P3 blends. For the P2 blend also quenching appeared, but less strong. *0-0*, *0-1*, *0-2* and *0-3* peaks appeared in the blend films at the same wavelength as in polymer only films.

In figure 5.12 the decay curves for blends, recorded at the *0-1* and *0-4* peak are shown. The decay observed at an emission wavelength of 545 nm shows quite similar behaviour and a double-exponential decay for all three blends. P2:ICBA is decaying slightly slower than the other two polymers. At 735 nm the emission from ICBA was detected. The P1 blend shows the slowest decay with 1.35 ns followed by P3 with 1.30 ns. Both of them show mono-exponential behaviour. The P2 curve shows the fastest decay and was fitted bi-exponentially with a short-lived component of 0.15 ns and a long-lived component of 1.20 ns. The decay at 735 nm depends on the surrounding ICBA.

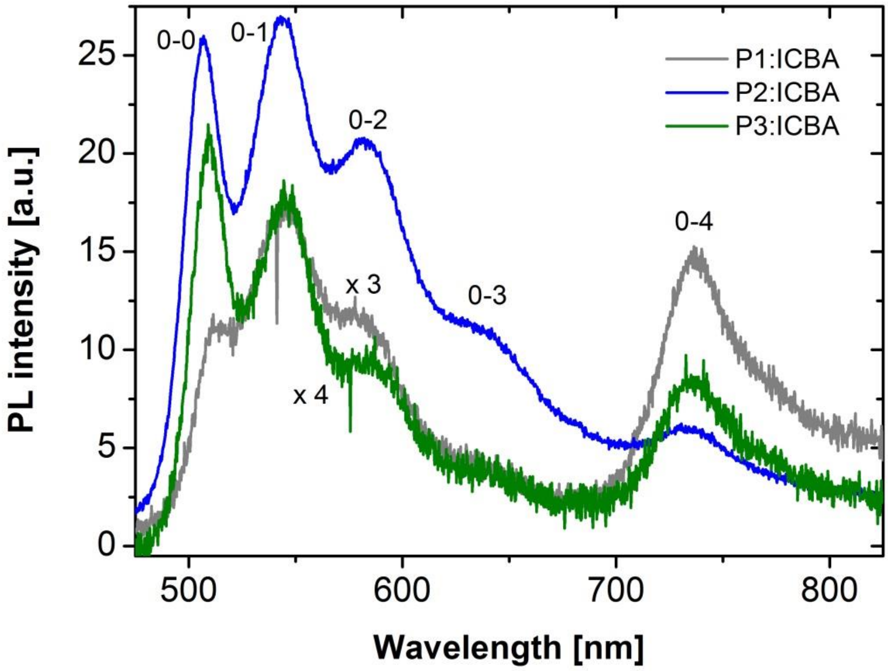

Figure 5.11: *PL emission curves derived from blends with a D/A weight ratio of 1:1*

Due to P1 showing the most crystalline behaviour, it seems like the ICBA tends to form clusters between the crystalline P1 regions. It has the slowest decay due to little interface between polymer and fullerene derivative. The amorphous P2 shows the fastest decay, which indicates that ICBA is well distributed in the polymer film. P3 shows an intermediate decay, probably due to ICBA cluster in the P1 regions and intercalation in P2 regions. For blends, (suggested) triplet formation seems to be reduced, as the lifetimes are clearly shorter as for polymer-only films. This indicates that charge transfer to the ICBA is efficient as competing process.

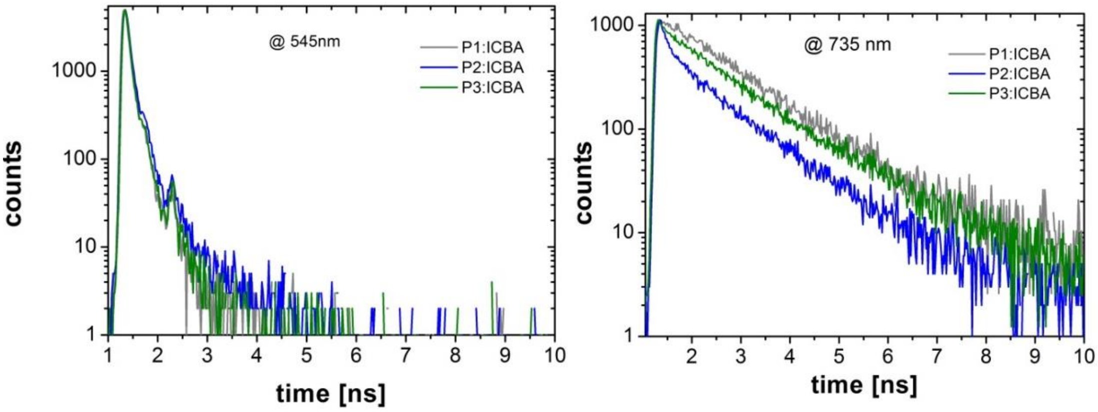

Figure 5.12: *TCSPS lifetime decay curves of blends with D:A of 1:1, detected at 545 nm (left) and 735 nm (right)*

In figure 5.13 the decay times for polymer only blends are summarized with filled dots and for blends with empty dots. There the short- and long-lived components of the decays are labelled. The short-lived components indicate excitons that recombined on the same polymer chain, where they were created. Long-lived components appear due to exciton moving to another polymer chain as they were created before they recombine and emit light.

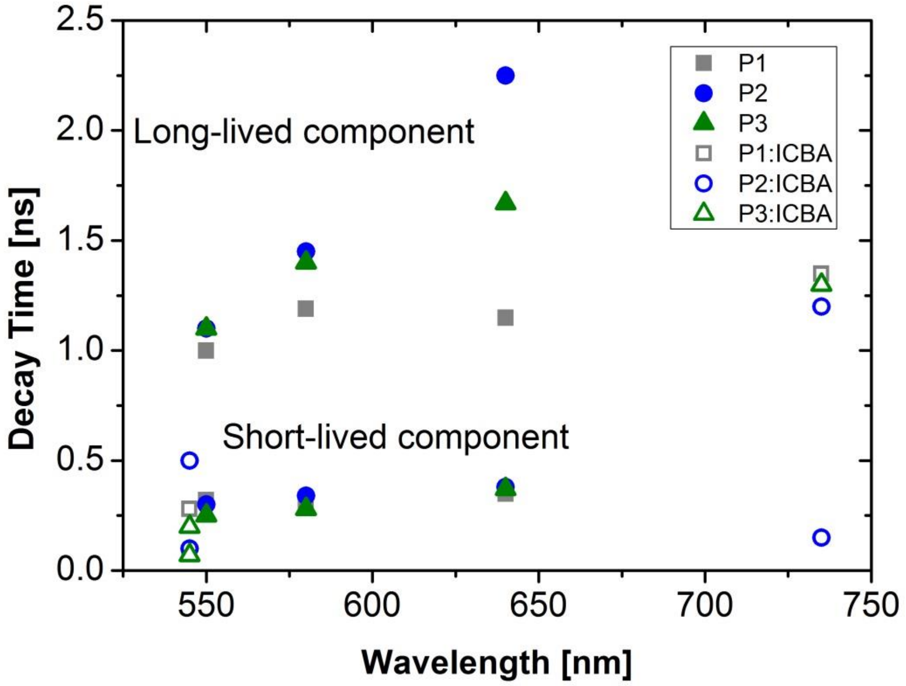

Figure 5.13: *Summarized decay times for polymer-only films and blends with a weight ratio of 1:1*

5.6 Optical characteristics

The optical absorption spectra are illustrated in figure 5.14 for F8T2:ICBA films with a weight ratio of 1:1 and figure 5.15 for a weight ratio of 1:4. The absorption coefficient (absorption divided by layer thickness) is plotted over wavelength. The spectra obtained are a quite complex superposition of the ICBA absorption (merely in UV) and the F8T2 absorption (with several peaks across the whole range). In detail, they show the highest peak in the ultra violet range at 200 nm. At 260 nm another peak appears and at 320 nm a shoulder is visible. The feature appearing in the visible range has two peaks at about 460 and 480 nm.

Figure 5.14 shows that the absorption coefficient exhibits higher values for P1 and P2, when the blends where annealed. This effect is the other way around for P3. In blends with a weight ratio of 1:4 the annealed blends of all three polymers show larger absorption coefficients. In both cases P2 is the strongest absorbing material, followed by P3 and P1 respectively. The ICBA is contributing only in the ultraviolet range.

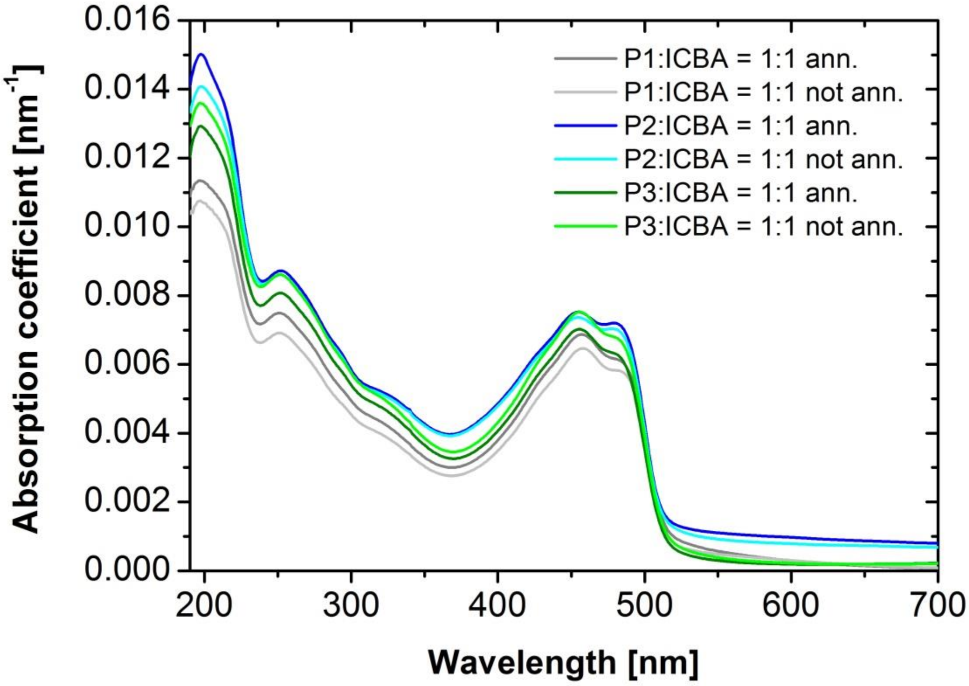

Figure 5.14: *Absorption coefficients for annealed and not annealed blends with a weight ratio of 1:1*

Figure 5.16 shows the normalized absorption peaks in the visible range for films fabricated from polymers-only. In figure 5.17 (1:1) and figure 5.18 (1:4) the normalized peaks for blends in the visible wavelength range are shown, to gain knowledge of shifts in the wavelength.

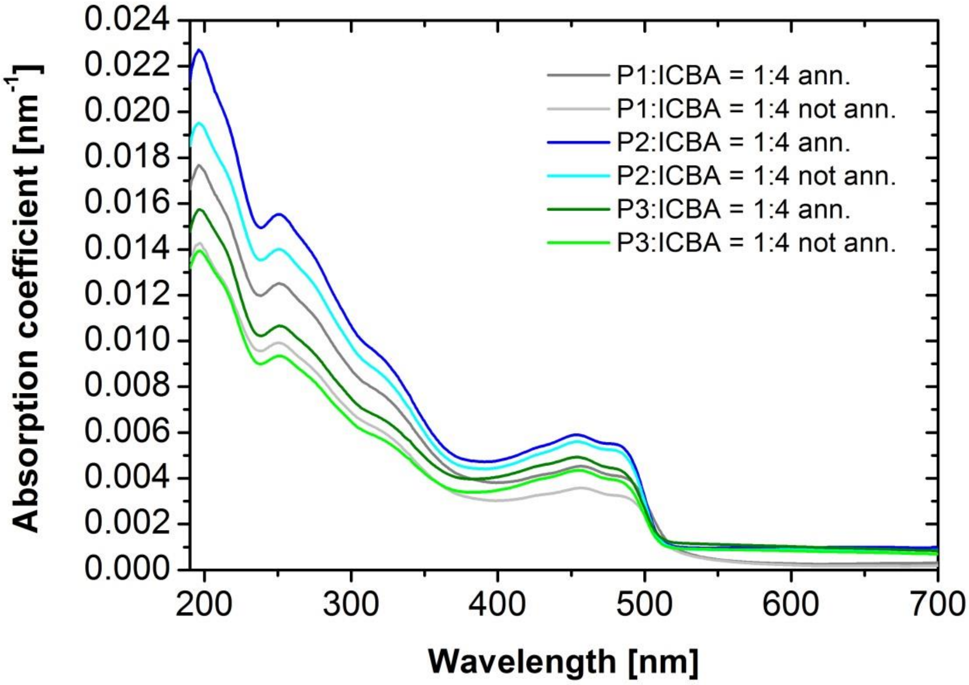

Figure 5.15: *Absorption coefficients for annealed and not annealed blends with a weight ratio of 1:4*

Having a look at the absorption behaviour of polymer only films, it shows that the *1-0* peak is located at 460 nm for all of the polymers, while the *0-0* peak is slightly blue-shifted for P2 compared to P1. The difference in height between *1-0* and *0-0* peak gives information about the order in the films. Thereby the two peaks show the least difference in the P2 blend, while it is increased for P3 and P1 respectively. Therefore P2 is least ordered and P1 most ordered, which matches the previous observations. P3 is at an intermediate stage, which reflects that this polymer is a mixture of P1 and P2 building blocks. For wavelengths above 550 nm a background remains (origin unknown), it is strongest for P2 and quite the same for P1 and P3.

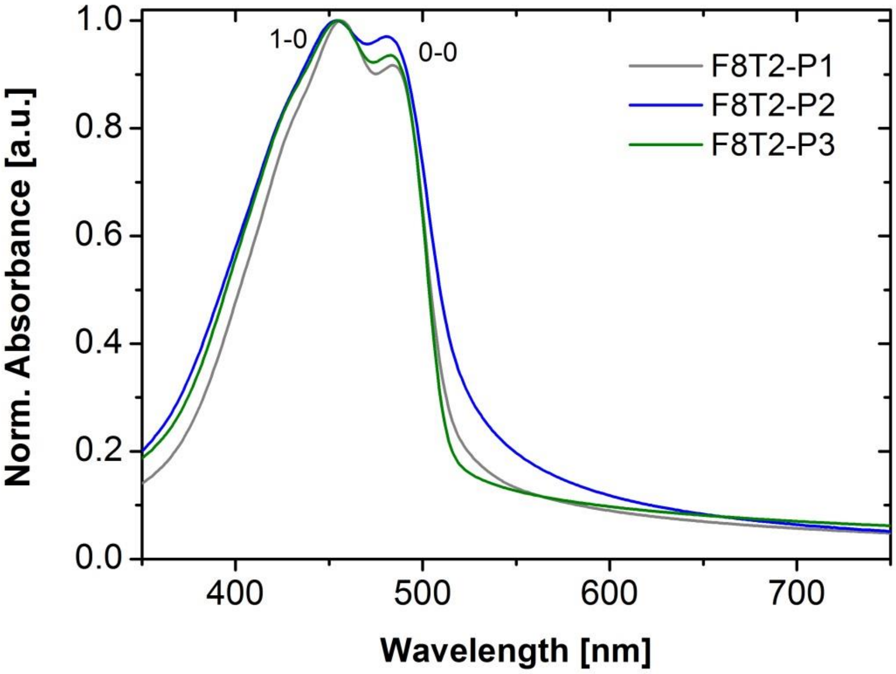

Figure 5.16: *Normalized absorption of polymer-only films*

The curves derived from blends with a weight ratio of 1:1 show a quite similar shape compared to the absorption curves measured from polymer only films. The *1-0* peak is not shifted either, but subtle shifts to the blue wavelength region for P2 and P3 are visible compared to P1. It seems like annealing of the films is not affecting the peak positions. The ratio of the *0-0* to *0-1* peak is increased for both P2 blends compared to P1 and P3 ones. But here, P3 does not appear as intermediate between the other polymers. This is indicated by the observation that in blends with a weight ratio of 1:1, P2 still exhibits the least order, but between P1 and P3 no difference appears anymore. What also changed compared to polymer only blends is that the rise of the peak is less steep. This shows a contribution of the acceptor material to the absorption spectrum. The background above 550 nm is again strongest for P2, followed by P1 and P3.

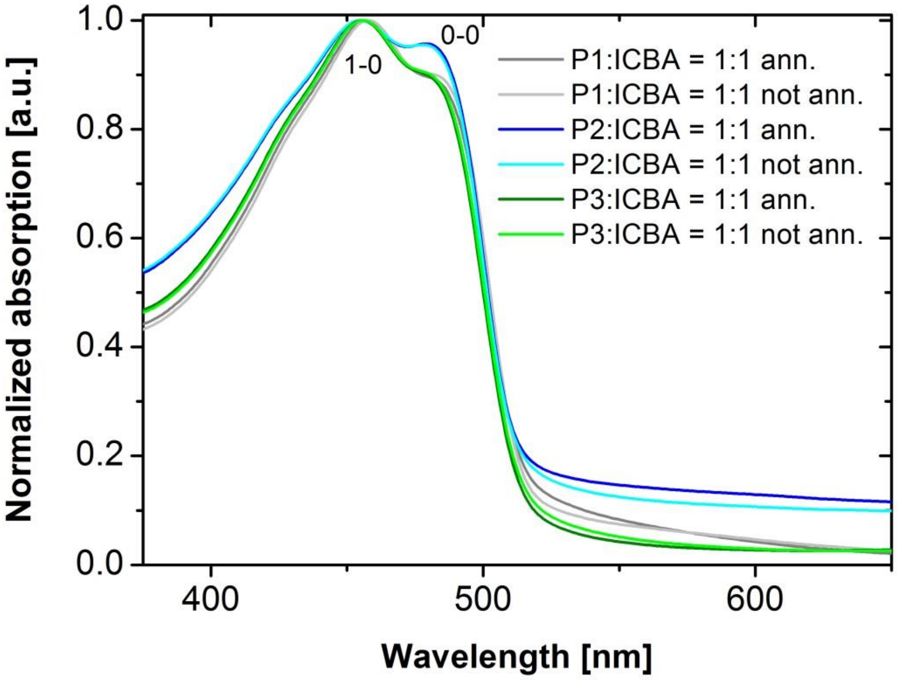

Figure 5.17: *Normalized absorption of annealed and not annealed blends with a weight ratio of 1:1*

For blends fabricated with a weight ratio of 1:4 the absorption curves are a little bit changing in shape. Positions and shifts of *0-0* and *0-1* peak have the same trends as for blends with a weight ratio of 1:1. Also the ordering behaviour inside the blends seems to be the same. What is different is that at around 430 nm a shoulder appears and more contribution from the ICBA is visible. The background has the largest values for P3 blends followed by P2 and P1, respectively.

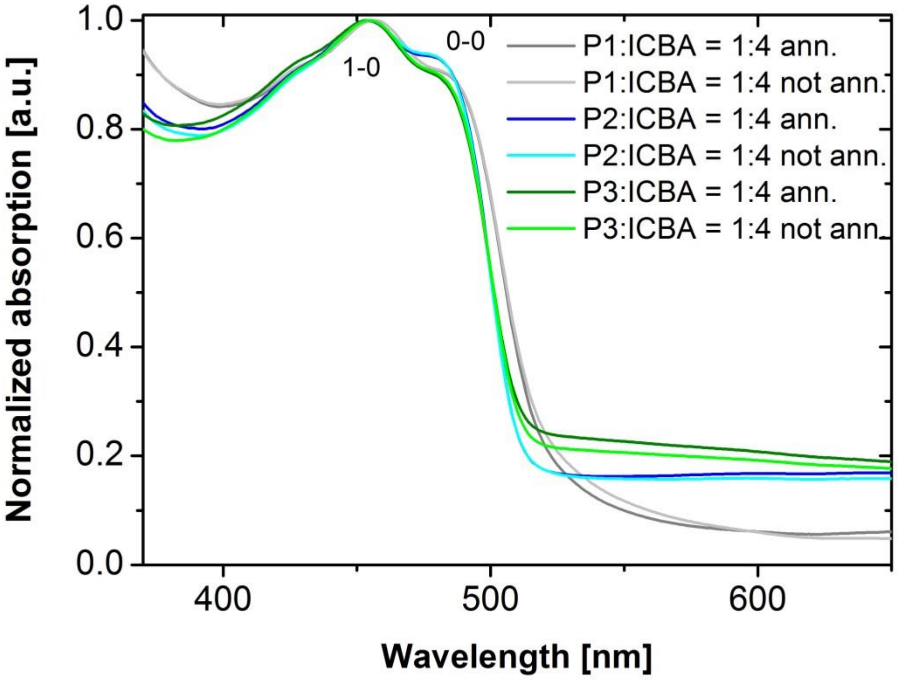

Figure 5.18: *Normalized absorption of annealed and not annealed blends with a weight ratio of 1:4*

5.7 Visual appearance of the blends

To investigate the macroscopic homogeneity of the active layer, optical microscopy pictures were taken. On the left hand side of figure 5.19, a pixel of a F8T2:ICBA solar cell with a D/A ratio of 1:1 and on the right side one with a ratio of 1:4 is shown. Both of these images were taken from P1 blends, but they are representative for blends fabricated from all three polymers. As clearly can be seen, there are only a few undissolved ICBA grains in blend films with a weight ratio of 1:1, where there are many more in 1:4 blends. In the latter, also larger agglomerates of the fullerene derivative appear with sizes much larger than 1 µm. Note: The light or dark circles surrounding the defects in the image are a result of local heating of the film, induced by strong local currents flowing due to short circuiting at the defects. This is seen here, because the microscopy investigation was done after measurement of the devices under simulated solar conditions.

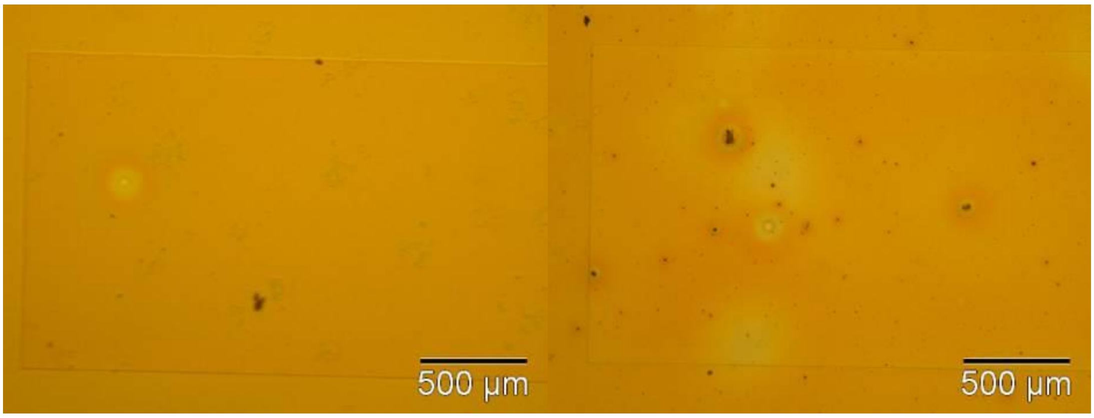

Figure 5.19: *Microscope pictures taken with a magnification of 50x of a blends with a weight ratio of 1:1 (left) and 1:4 (right)*

5.8 Blend surface morphology and phase separation

Blend morphology investigations via AFM were done only for F8T2:ICBA films with a donor-acceptor ratio of 1:1, because light microscopy showed large agglomerates in the 1:4 films, unsuitable for AFM. The topographical images can be seen in figure 5.20, where annealed and pristine blend of each polyfluorene are opposed to each other. The same was done for phase images as shown in figure 5.21.

Topography images:

The pristine P1 blend has a quite rough surface, where features have sizes of around one hundred nanometres. A refined topography is obtained for the annealed blend. Features on the surface are easier to distinguish. P2 blends show amorphous behaviour, with large feature sizes of around 200 nm. The annealed blend shows no clear change of the film morphology. The character and the feature sizes seem to stay the same. This blend is therefore the most amorphous one (no reorganisation tendency). For pristine P3, a lamellar-looking structure appears where single features appear in an oval kind of shape. Annealing is completely changing the topographic structure. It seems to dissolve these fibre-like features. Instead round features appear, with sizes of 100 nm and below.

The images clearly show different surface morphologies for the blends fabricated from the three different polymers.

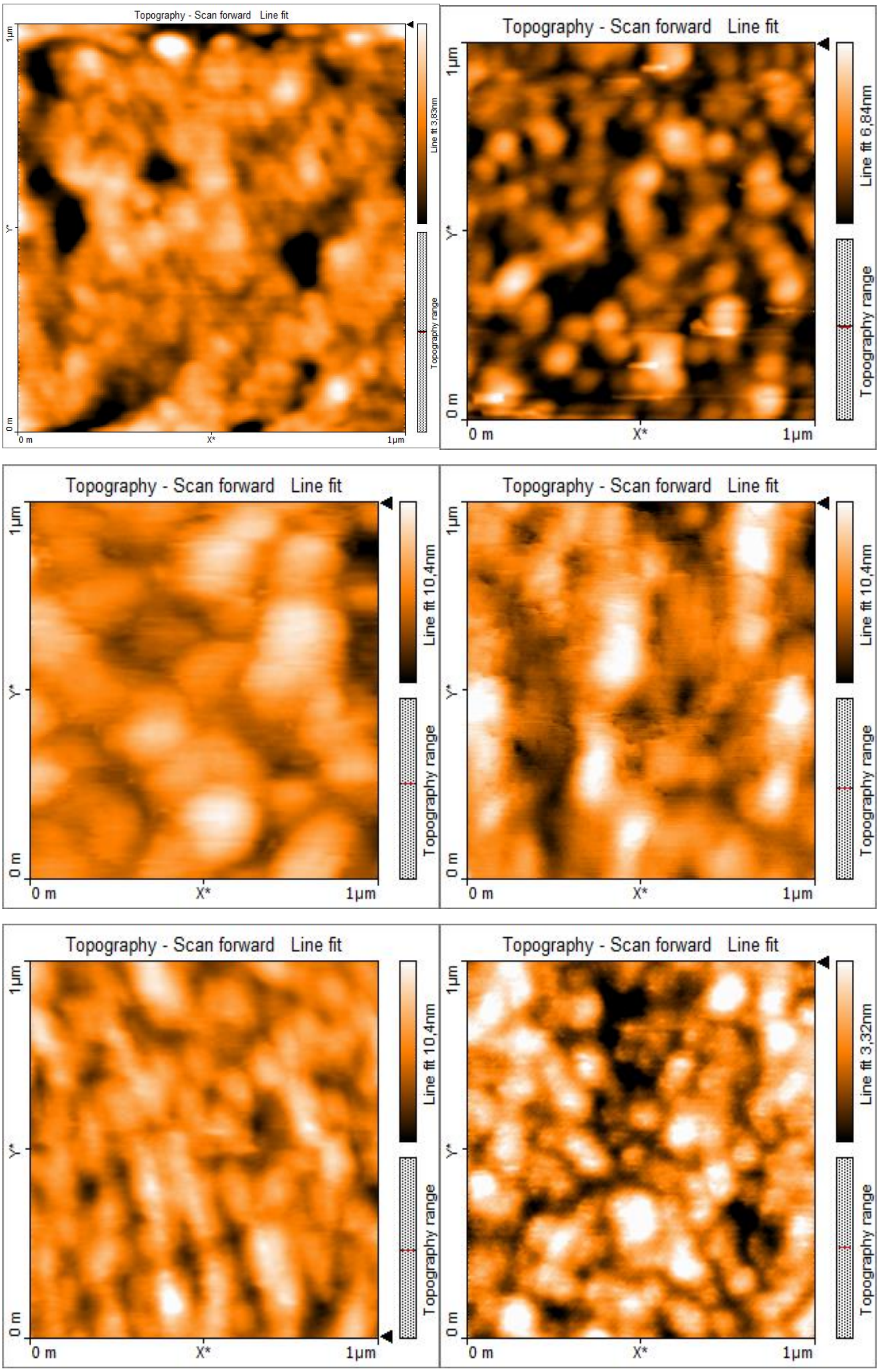

Figure 5.20: *AFM topography images taken from blends with a weight ratio of 1:1 (top, left: P1 not annealed; top, right: P1 annealed; middle, left: P2 not annealed; middle, right: P2 annealed; bottom, left: P3 not annealed; bottom, right: P3 annealed)*

Phase images:

Investigation of the phase composition of the untreated P1 film shows some kind of a branched structure of the polymer, with “dark” parts of ICBA that are distributed around the polymer (note: phase in AFM is induced by topographical features and different hardness of the surface; it is suggested that the darker regions represent the softer and more mobile material, therefore assigned to ICBA). The annealed blend exhibits definitely phase separated regions. It looks like the polymer forms round shaped features and ICBA filling up the free space in between. The image taken from the pristine P2 blend shows equally sized phase separations of foliate-like structure. Also here, the dark parts around these structures indicate ICBA-rich areas. The features have sizes of about 200 nm. That changes for the annealed blend of the same polymer. The quite ordered structure was changed to an image where sharp peaks in the surface are visible. Due to that the picture is quite noisy. The phase images of both P3 blend are reflecting the topography images really well, as fibre-like phases of donor and acceptor material appear for pristine films. The annealed one shows smaller, round features of polymer that are distributed in no certain order. The fullerene derivative appears again as the dark areas.

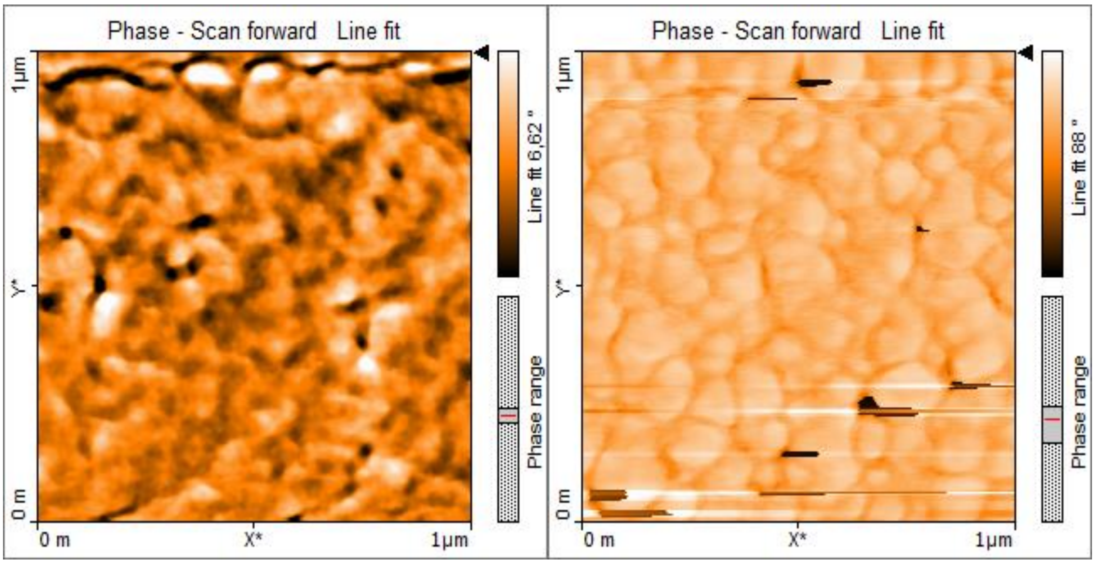

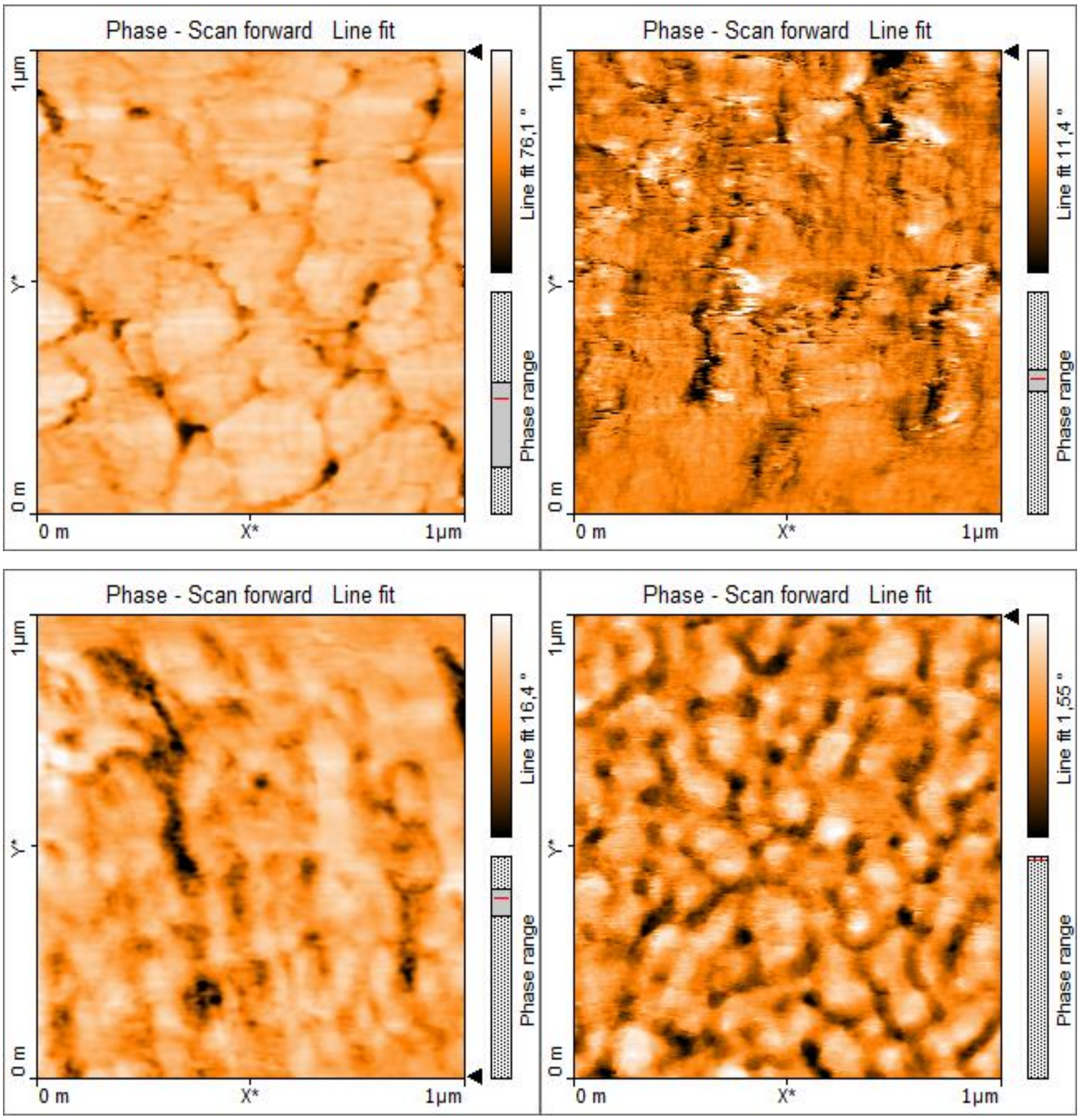

Figure 5.21: *AFM phase images taken from blends with a weight ratio of 1:1 (top, left: P1 not annealed; top, right: P1 annealed; middle, left: P2 not annealed; middle, right: P2 annealed; bottom, left: P3 not annealed; bottom, right: P3 annealed)*

5.9 Molecular order and orientation

In figure 5.22 grazing incidence X-ray diffraction measurements of drop casted samples from all three polymers are shown. The x-axis is labelled with the in-plane scattering vector where the y-axis is labelled with the out-of-plane scattering vector. Intensities are illustrated by a logarithmic colour code. It starts with blue for low intensities and goes to red for high ones. In figure 5.23 plots of the same measurements are shown, but in this case intensity over $|q|$. The absolute value of q was calculated by $|q| = \frac{4\pi}{\lambda}\sin\theta$, where λ=1 Å and θ is the scattering angle.

P1: In figure 5.22 plot (top, left) two rings are visible: a sharp one at 0.4 Å^{-1} and a broad one at 1.4 Å^{-1}. These rings are characteristic for the separation of the side chains in F8T2 thin films. The smaller one indicates the distance of the polymer backbones with side chains in between. The other one shows the distance of the side backbones without side chains in between. Due to this ring having quite the same intensity for large and small q_z values, there is no preferred orientation. The red dots in this plot display probably silicon dust. In figure 5.23 the same three features can be seen for P1. The ring at 0.4 shows a sharp, narrow peak in this illustration, with an intensity of about 4500 counts. The second ring is a quite broad feature with an intensity of 6500 counts. The surface contamination shows up as a small, kinky peak at 2.0 Å^{-1}, which matches the value for Si (111).

P2: For P2 the measurements (figure 5.22, tor, right) show that the smaller ring vanishes and the larger one gets shifted to the right to 1.5 Å^{-1}, but has with 4000 counts a lower intensity than for P1. This indicates more parallel stacking of the polymer backbones. What can be also seen in the measurement of P2 is that the larger ring has its highest intensity at large q_z values. This shows a preferred polymer orientation dependence parallel to the substrate. The narrow, but distinct ring at about 2.1 Å^{-1} that appears in this plot is a signal from silicon that might come from breaking the substrate. It shows up as a very small peak in figure 5.23. What is also clearly visible is a distinct feature with high intensity at about 0.8 Å^{-1}. This probably comes from residues from the synthesis and is definitely not a signal from an organic material.

P3: Figure 5.22 (bottom, left) shows no ring at 0.4 Å^{-1} as well, which means that the order in this arrangement is broken and parallel stacking of the backbone is preferred. The second ring shows with 3500 counts less intensity than for P2 and is according to figure 5.23 a little bit shifted back to the left to a value of 1.45 Å^{-1}. This means less parallel stacking compared to P2 and more herringbone structure. As for P2 it has the highest intensity at large q_z values. So the preferred polymer orientation is parallel to the substrate as well.

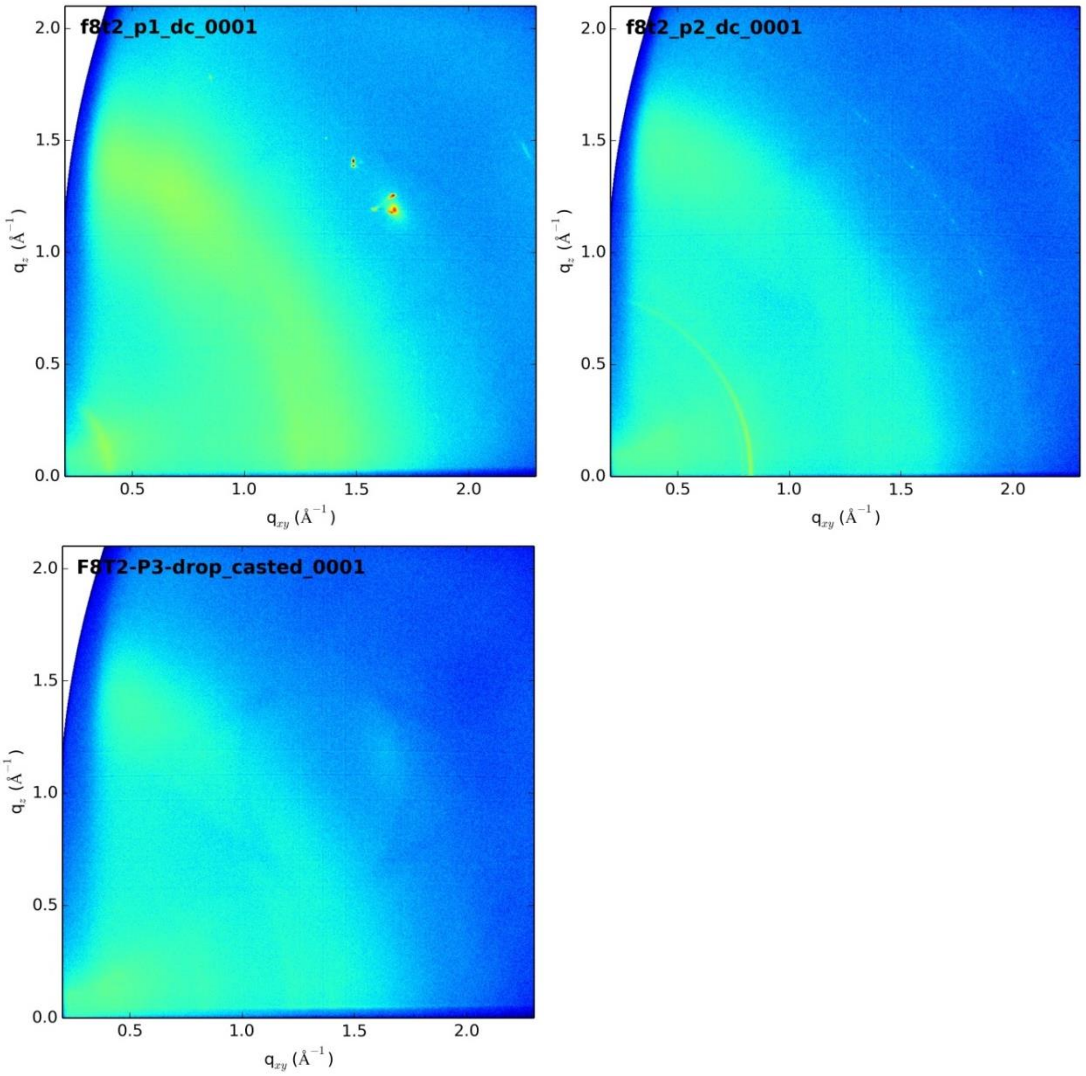

Figure 5.22: *Illustration of the in-plane over the out-of-plane scattering vector in a logarithmic colour code derived from drop casted polymer only films (P1: top, left; P2: top, right; P3: bottom, left)*

With the positions of the diffraction rings, which are derived from the peaks in figure 5.23 the d-spacings d (spacing between adjacent lattice planes) can be calculated via:

$$\frac{2\pi}{|q|} = d \tag{5}$$

The values can be found in table 5.3. The d-spacings detected for P1 are matching the results for X-ray diffraction under grazing incidence conditions for F8T2 thin films reported by Werzer et al. [44] very well. Due to Kinder et al. [45] the backbones of F8T2 lie in the plane of the substrate. So the d-spacing of about 16 Å is associated with the layering distance between sheets of polymer chains. This layering happens because of the segregation of the backbones from the main chain from aggregated side chains. The smaller peak for d-spacings of around 4.5 Å could indicate the lateral distance between polymer chains in the formed layer. Another explanation could be the crystallization of the side chains.

Table 5.3: *Detected absolute values q and calculated d-spacings*

Polymer	|q| (Å^{-1})	d (Å)
P1	0.40 1.40	15.7 4.5
P2	1.50	4.2
P3	1.45	4.3

For P2 and P3 the d-spacing at around 4.5 Å is visible but the other one at around 16 Å disappears. That means that the order of the layering of the polymers backbones is getting lost for branched side chains.

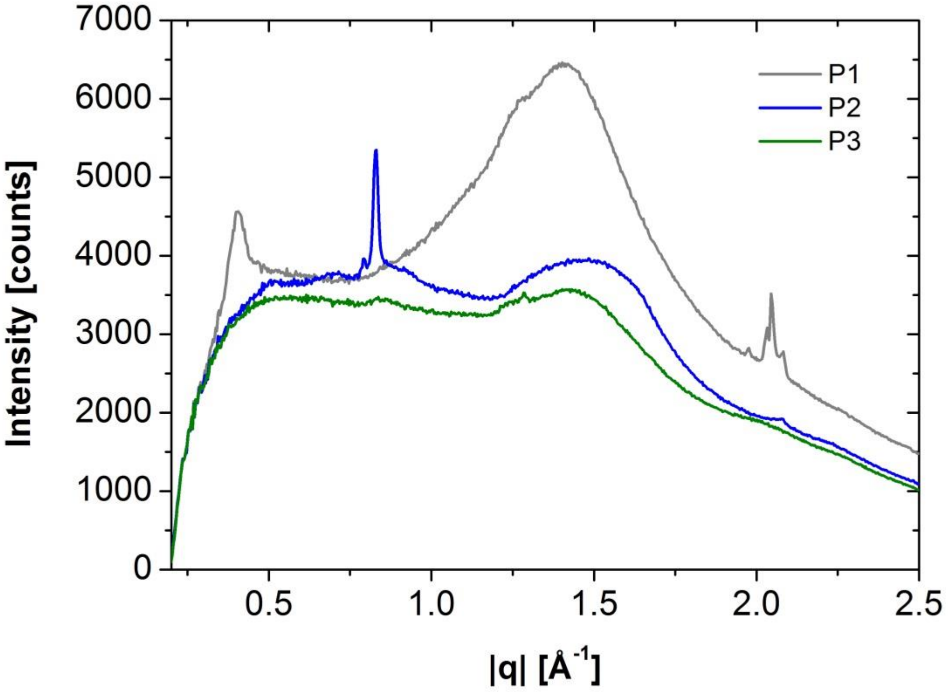

Figure 5.23: *Illustration of the intensity over the absolute value of the scattering vector derived from drop casted polymer only films*

5.10 Conclusions

For blends fabricated with three different types of F8T2 as donor material and ICBA as acceptor material (D/A weight ratio of 1:1 and 1:4) and sole polymer films, different electrical, optical and morphological investigations have been performed. Photocurrent measurements revealed current densities for all material combinations with values up to -0.3 mA/cm^2 and open circuit voltages between 0.8 and 1.0 V. The photoconversion efficiencies reached values of 0.1%. EQE measurements showed peak values of up to 0.5 %, and clear peak shifts, which reveal that blends fabricated from P1 produced the most crystalline and from P2 the least crystalline films. The emission dynamics showed triplet formation for polymer-only films as they exhibit slow decay times. For blends, efficient quenching and probably polaron formation were observed. Electroluminescence measurements indicated a charge transfer state arising at wavelengths of 800 nm and above. The recorded absorption spectra showed a maximum in the visible range at about 450 nm from the F8T2 and from the ICBA only a contribution in the ultraviolet range. Also here, peak shifts show that P1 films are the most ordered ones, while P2 films have the least order. AFM morphology investigations clearly revealed a phase separation between donor and acceptor material with domain sizes between 100 and 200 nm. The molecular order of polymer only films was investigated by grazing incidence X-ray diffraction. All three polymers showed signs of crystallization behaviour of the side chains, but only P1 exhibited a characteristic order in the stacking distance between sheets of polymer chains.

The device performances appear low, compared to similar reported material systems. This might be due to a considerable concentration of palladium impurities in the polymers, a residue of the synthesis, where it was used as a catalyst. Nevertheless, a clear impact of the different ordered side chains on the ability to crystallization has been found, which reflects also in the photovoltaic performance.

A Appendix

A.1 List of abbreviations

HOMO = highest occupied molecular orbital
LUMO = lowest unoccupied molecular orbital
BHJ = bulk hetero junction
SCLC = Space charge limited current
EQE = external quantum efficiency
AFM = atomic force microscope
TCSPC = time correlated single photon counting
XRD = X-Ray diffraction
F8T2 = Poly (9,9-dioctylfluorene-cobithiophene)
ICBA = indene-C_{60} bisadduct
PCBM = phenyl-C_{70}-butyric acid methyl ester
ITO = Indium tin oxide
IPA = Isopropyl alcohol
1,2 DCB = 1,2-dichlorobenzene
V_{OC} = open circuit voltage
J_{SC} = short circuit current density
FF = fill factor
EQE = External quantum efficiency

A.2 List of illustrations

A.3 List of tables

A.4 Bibliography

[1] C. Brabec, V. Dyakonov und U. Scherf, Organic Photovoltaics - Materials, Device Physics, and Manufacturing Technologies, Wyley-VCH, 2008.

[2] “Our Climate,” [Online]. Available: http://www.ourclimate.net/altenergy.htm. [Accessed 27 10 2014].

[3] Y. Li und Y. Zou, „Conjugated Polymer Photovoltaic Materials with Broad Absorption Band and High charge Carrier Mobility,“ *Advanced Materials,* pp. 2952-2958, 2008.

[4] D. Wöhrle und D. Meissner, „Organic Solar Cells,“ *Advanced Materials,* 1991.

[5] M. A. Green, K. Emery, Y. Hishikawa, W. Warta and E. D. Dunlop, “Solar cell efficiency tables (version 44),” *Progress in Photovoltaics,* 2014.

[6] C. W. Tang , „Two-layer organic photovltaic cell,“ *Applied Physics Letters,* 1985.

[7] J. H. Schön, C. Kloc und B. Batlpgg, „Efficient photovoltaic energy conversion in oentacene-based heterojunctions,“ *Applied Physics Letters,* 2000.

[8] A. L. J. Richard, Soft Condensed Matter, Oxford University Press, 2003.

[9] G. Strobl, The Physics of Polymers, Springer, 2010.

[10] H. W. Kroto, J. R. Heath , S. C. O’Brien , R. F. Curl and R. E. Smalley, “C-60 - Buckminsterfullerene,” *Nature,* 1985.

[11] B. Valeur and M. N. Berberan-Santos, Molecular Fluorescence, WILEY-VCH, 2013.

[12] B. C. Yadav and R. Kumar, “Structure, properties and applications of fullerenes,” *International Journal of Nanotechnology and Applications,* 2008.

[13] D. Kim and L. Minyung, “Observation of Fluorescence Emission from Solutions of C_60 and C_70 and Measurement of their Excited-State Lifetimes,” *American Chemical Society,* 1992.

[14] T. Zhuang, X.-F. Wang, T. Sano, Z. Hong, Y. Yang and J. Kido, “Fullerene derivatives as electron donor for organic photovoltaic cells,” *Applied Physics Letters,* 2013.

[15] S. K. M. Jönsson, J. Birgerson und X. Crispin, „The effects of solvents on the morphology and sheet resistance in poly(3,4-ethylenedioxythiophene)–polystyrenesulfonic acid (PEDOT–PSS) films,“ *Synthetic Metals,* 2003.

[16] B. Friedel, P. E. Keivanidis und T. J. Brenner, „Effects of Layer Thickness and Annealing of PEDOT:PSS Layers in Organic Photodetectors,“ *Macromolecules,* 2009.

[17] F. Padinger, R. S. Rittberger and N. S. Sariciftci, “Effects of Postproduction Treatment on Plastic Solar Cells,” *Advanced Functional Materials,* 2003.

[18] A. Moliton und J.-M. Nunzi, „How to model the behaviour of organic photovoltaic cells,“ *Polymer International,* 2006.

[19] “http://www.academia.edu,” [Online]. Available: http://www.academia.edu/245548/bulk_heterojunction_solar_cells. [Zugriff am 26 3 2014].

[20] C. J. Brabec, „Organic photovoltaics: technology and market,“ *Solar Energy Materials & Solar Cells,* 2004.

[21] H. Hoppe and N. S. Sariciftci, “Organic solar cells: An overview,” *Journal of Materials Resarch,* 2004.

[22] S. Günes, H. Neugebauer and N. S. Sariciftci, “Conjugated Polymer-Based Organic Solar Cells,” *Chemical Review,* pp. 1324-1338, 2007.

[23] A. Pein, *Synthesis and Characterization of Materials for Optoelectronic Devices,* Graz, 2011.

[24] “Portal für organische Chemie,” 22 09 2014. [Online]. Available: Available: http://www.organische-chemie.ch/OC/Namen/Suzuki.htm.

[25] J.-H. Huang, C.-Y. Yang and Z.-J. Ho, “Annealing effect of polymer bulk heterojunction solar cells based on polyfluorene and fullerene blend,” *Organic Electronics,* pp. 27-33, 2 2009.

[26] V. D. Mihailetchi, W. P. Blom, J. C. Hummelen und M. T. Rispens, „Cathode dependence of the open-circuit voltage of polymer:fullerene bulk heterojunction solar cells,“ *Journal of Applied Physics,* 2003.

[27] N. A. D. Yamamoto, A. G. Macedo and L. S. Roman, “Thickness Effeect on F8T2/C_60 Bilayer Photovoltaic Devices,” *Journal of Nanotechnology,* 2012.

[28] “Wikimedia,” [Online]. Available: http://upload.wikimedia.org/wikipedia/commons/5/54/Solarcelliqe.png. [Accessed 17 10 2014].

[29] D. Abou-Ras, T. Kirchartz and U. Rau, Advanced Characterization Techniques for Thin Film Solar Cells, Weinheim, Germany: WILEY-VCH, 2011.

[30] „KF Universität Graz,“ [Online]. Available: http://www.uni-graz.at/klaus.zangger/GdS.pdf. [Zugriff am 27 3 2014].

[31] G. R. Strobl, The Physics of Polymers - Concepts for Understanding Their Structures and Behaviour, Springer, 2007.

[32] "Fakultät für Physik Universität Regensburg," [Online]. Available: http://www.physik.uni-regensburg.de/forschung/schwarz/Mikroskopie/11-AFM.pdf . [Accessed 24 3 2014].

[33] "Connexions," [Online]. Available: http://cnx.org/content/m22326/latest/?collection=col10719/latest. [Accessed 24 3 2014].

[34] B. K. Tanner, T. P. A. Hase, T. A. Lafford and M. S. Goorsky, "Grazing Incidence In-Plane X-Ray Diffraction in the Laboratory," *Advances in X-Ray Analysis,* 2004.

[35] Bruker axs, [Online]. Available: mmlab.dlut.edu.cn/training/gid.pdf. [Accessed 24 10 2014].

[36] "Neutron Scattering Group, AMES Laboratory," [Online]. Available: http://www.reflec.ameslab.gov/gid.php. [Accessed 24 10 2014].

[37] "Ossila," [Online]. Available: http://www.ossila.com/oled_opv_ofet_catalogue3/PCDTBT_P3HT_PCBM_PEDOT_PSS_for_organic_photovoltaics/M181-ICBA.php . [Accessed 20 3 2014].

[38] "Ossila," [Online]. Available: http://www.ossila.com/oled_opv_ofet_catalogue3/PCDTBT_P3HT_PCBM_PEDOT_PSS_for_organic_photovoltaics/M123-PEDOT-PSS-PJet%28OLED%29.php. [Accessed 06 10 2014].

[39] "ABET Technologies," [Online]. Available: http://www.abet-technologies.com/solar-simulators/low-cost. [Accessed 3 10 2014].

[40] "UC Davis College of Engineering," [Online]. Available: http://research.engineering.ucdavis.edu/cnm2/analysis-and-characterization/dektak-iia/. [Accessed 23 09 2014].

[41] D. Kriegner, E. Wintersberger and J. Stangl, “xrayutilities: a versatile tool for reciprocal space conversion of scattering data recorded with linear and area detectors,” *Journal of Applied Crystallography,* 2013.

[42] J.-H. Huang, C.-P. Lee, Z.-Y. Ho, D. Kekuda, C.-W. Chu and K.-C. Ho, “Enhanced spectral response in polymer bulk heterojunction solar cells by using active materials with complementary spectra,” *Solar Energy Materials & Solar Cells,* 2009.

[43] E. T. Hoke, K. Vandewal, J. A. Bartelt, W. R. Mateker, J. D. Douglas, R. Noriega, K. R. Graham, J. M. J. Fréchet, A. Salleo and M. D. McGehee, “Recombination in Polymer:Fullerene Solar Cells with Open-Circuit Voltages Approaching and Exceeding 1.0 V,” *Advanced Energy Materials,* 2013.

[44] O. Werzer, H.-G. Flesch, D.-M. Smilgies and R. Resel, “Temperature Induced Structural Evolution of a Fluorene-Thiophene Copolymer on Rubbed Surfaces,” *Journal of Polymer Science Part B: Polymer Physics,* 2009.

[45] L. Kinder, J. Kanicki, J. Swensen und P. Petroff, „Structural ordering in F8T2 polyfluorene thin-film transistors,“ in *Proceedings of SPIE Vol. 5217,* Bellingham, WA, 2003.